Master of Science Thesis in Electrical Engineering
Department of Electrical Engineering, Linköping University, 2021

The relation between rolling resistance and tyre temperature in real driving scenarios

Hugo Jansson and Martin Åsenius

LINKÖPING UNIVERSITY

Master of Science Thesis in Electrical Engineering

The relation between rolling resistance and tyre temperature in real driving scenarios:

Hugo Jansson and Martin Åsenius

LiTH-ISY-EX--21/5406--SE

Supervisor: **Docent Sogol Kharrazi**
ISY, Linköpings universitet & VTI
Doktorand Lisa Ydrefors
VTI

Examiner: **Associate Professor Jan Åslund**
ISY, Linköpings universitet

Division of Automatic Control
Department of Electrical Engineering
Linköping University
SE-581 83 Linköping, Sweden

Abstract

A large portion of the world's total emissions is caused by the transport sector where rolling resistance is one of the contributing factors. The inner tyre temperature is a factor that greatly influences the rolling resistance. The effect of temperature and rolling resistance is often examined in standardised tests carried out in a lab environment. In this work, field tests were carried to find out typical operating temperatures in real driving scenarios. The field tests were carried out on one set of A-class tyres and one set of B-class tyres at different speeds: city-, small country road-, large country road- and motorway driving. Tests were performed in varying ambient temperatures and weather conditions. The results show that the rear inner tyre temperature varies between 11 – 36°C in the spring around Linköping in Sweden.

A brush model was also developed to see how accurately the rolling resistance could be predicted. With springs, dampers, and Coulomb friction elements the behaviour of rubber was captured. The final model contains five model parameters that were estimated by parameter fitting to measurement data, using optimisation. Measurements were carried out at a test rig that measures the forces acting on the tyre. The measurements were performed for both the A-class and B-class tyre at two different temperatures corresponding to the findings from the field tests. The results show that the developed model has a promising correlation with the measurements for all loads and speeds that were tested.

Acknowledgments

We would like to extend our gratitude to VTI which has given us the possibility to challenge our engineering knowledge in such an interesting field.

A special thanks to Sogol Kharrazi who thoroughly have read our report and supplied a lot of input on where improvements were needed, to Lisa Ydrefors who helped us with measurements and input on our work and to Mattias Hjort who provided help when it was needed the most.

Thanks to all personnel in both the workshop and measurement lab at VTI, who helped us get all the equipment in order.

We would also like to thank our examiner Jan Åslund for input and fruitful meetings about our work.

Linköping, June 2021
Hugo Jansson and Martin Åsenius

Contents

Notation

Nomenclature

Symbol	Meaning
C_r	Rolling resistance coefficient
F_r	Rolling resistance, represented as a longitudinal force
RRM	Rolling resistance moment
CTC	Centre of Tyre Contact
F_z	Force in the z-direction at a distance e from the CTC
F_b	Force from one bristle
F_{ve}	Viscoelastic part of the bristle force
$F_{ve,z}$	Viscoelastic contribution to the F_z force
$M_{ve,y}$	Viscoelastic contribution to the RRM moment
F_f	Friction part of the bristle force
$\tilde{F}_f$	Trial force for the friction model
F_e	Elastic force from viscoelastic model
F_v	Viscous force from viscoelastic model
t	Time
τ	Time step
φ	Angular position of the bristle
ω	Rotational speed of the wheel
θ	Segment angle
δ	Deformation of tyre or bristle
δ_{k_1}	Spring deformation used in viscoelastic model
v	Velocity of tyre
α	Side slip angle
γ	Camber angle
R_l	Loaded tyre radius
R_e	Effective rolling radius
R_u	Unloaded rolling radius
e	Distance from CTC to the effective acting point of F_z
Δx	Distance from bristle to CTC

1 Introduction

1.1 Background

Environmental problems are one of the world's greatest challenges which will result in catastrophic events for a large part of humanity if they are not solved. Greenhouse gas emissions is one of the problems targeted and the transport sector stands for 27% of the emissions in Europe [5]. Rolling resistance stands for 4-7% of the total fuel consumption for passenger cars and a lowering of the rolling resistance by 10% could lead to a decrease of fuel consumption by 1-2% [6]. Since a decrease in rolling resistance reduces the amount of power required by the driveline the lowered fuel consumption depends on the efficiency of the driveline.

Efforts to understand rolling resistance have been made but the complex hysteresis losses of a pneumatic tyre are a challenging subject. To further increase the knowledge in the field this thesis investigate how rolling resistance is influenced by real driving tyre temperatures.

The term rolling resistance can be seen as an energy and in literature it is sometimes referred to as rolling loss instead of rolling resistance. In [15] the following formulation for rolling loss is formulated: *"Rolling loss is the mechanical energy converted into heat by a tire moving for a unit distance on the roadway"*. According to the definition, the unit of rolling loss becomes *Joule/mass*. It can be convenient in certain applications to consider the rolling loss as a vector instead of a scalar. In this thesis the term rolling resistance will be used to describe the force opposing the direction of travel, it is denoted F_r and have the unit N.

Rolling resistance is caused by an uneven distribution of the force the road is applying to the tyre. The displacement of the force occurs due to hysteresis in the rubber. The force in the z direction is shifted forward on the tyre in the direction

of travel, see figure 1.1. It results in a moment around the y-axis of the wheel, called rolling resistance moment (RRM), which opposes the direction of travel. When a tyre is exposed to deformation it returns to its original state. The return to its original state occurs with a time delay which results in hysteresis. The rolling resistance is influenced by the propulsion of the vehicle, the wheel pair with propulsion gives a higher rolling resistance compared to the free-rolling tyres [15]. In this thesis, only free-rolling tyres are considered.

$$RRM = F_z \, e \tag{1.1}$$

F_r is another way to describe the rolling resistance, with a force acting in the x-direction on the tyre.

$$F_r = \frac{RRM}{R_l} \tag{1.2}$$

The rolling resistance coefficient is defined as the ratio of F_r and the normal load on the tyre, F_z.

$$C_r = \frac{F_r}{F_z} \tag{1.3}$$

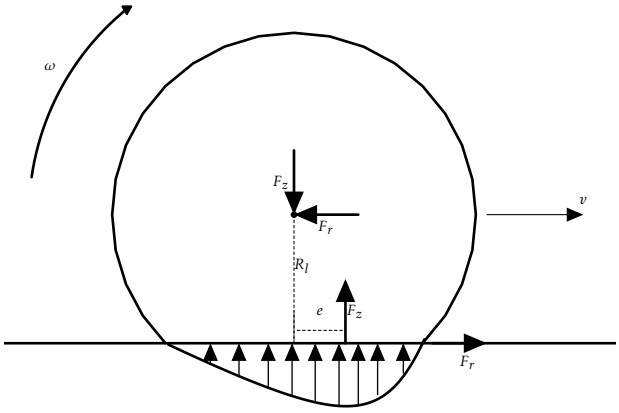

Figure 1.1: *The different forces acting on the tyre.*

Definitions of coordinate systems for the tyre is stated in figure 1.2. The coordinate system is set according to ISO 8855 [14] where index R stands for road and index w for wheel. γ and α are the camber angle and the sideslip angle. The camber- and sideslip angles are not considered in this thesis and are set to zero.

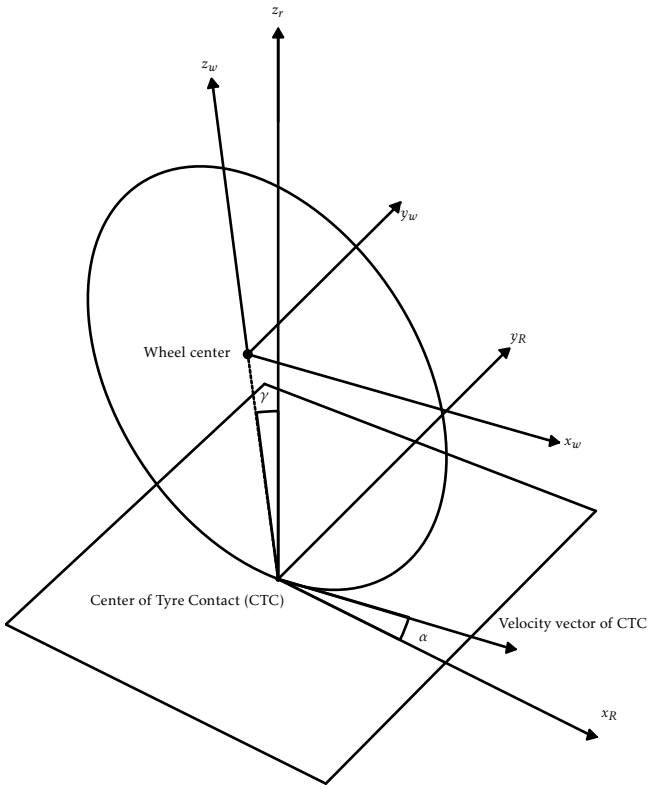

Figure 1.2: *Coordinate system of the wheel.*

1.2 Problem description

The main objective of this thesis is to investigate how different tyre temperatures influence the rolling resistance and in what range the temperature of a normal passenger car tyre operates within. The goal is to create a model predicting rolling resistance which is accurate at several different tyre temperatures. The resulting problem formulation becomes straightforward:

- How do different tyre temperatures influence the rolling resistance?
- Within what temperature range does the tyre of a passenger car operate?
- How accurately can a model predict the rolling resistance of a tyre at different tyre temperatures?

1.3 Approach

In this thesis, measurements in real traffic scenarios are collected to find out in what range of temperatures a tyre operates at different speeds and ambient conditions. A model that includes the rolling resistance of a tyre is derived. A set of parameters of the model is adapted to fit data of rolling resistance at different tyre temperatures. The data is acquired from a free-rolling tyre. The temperature measurements in real traffic scenarios are therefore mainly focused on the rear tyres since they are also free-rolling tyres.

1.4 Related research

Rolling resistance of pneumatic tyres has been of interest for at least the last 50 years. A lot of factors influence the rolling resistance which gives the opportunity to approach the problem in many ways. There is also a lot of research within the area of modelling rolling resistance which has been done with different approaches.

A review of different rolling resistance models can be seen in [11]. These models are ranging from simple brush models to extensive empirical models and finite element models.

Research on how temperature and speed influence the rolling resistance when equilibrium temperature is reached in tyres has been covered extensively in the literature. How the rolling resistance is influenced when the tyre is not in equilibrium is a far less researched area. This is the focus in [12] where the influence of transient speed changes and associated temperature changes are discussed and a model taking this into account when calculating the rolling resistance is presented. A tyre normally starts at ambient temperature and is then exposed to deformation while rolling, causing hysteresis in the rubber. When driving at a constant speed the tyre is continuously heated up until it reaches an equilibrium temperature. When increasing the speed, the rate of deformation increases thus leading to more heat generation and higher temperatures. For a passenger car tyre, the equilibrium temperature is reached after around 30 minutes and occurs due to that the tyre is heated up by hysteresis and cooled down from heat exchange with its surroundings at an equal rate. The rolling resistance is dependent on the temperature of the tyre due to the material behaviour in rubber, with a higher temperature a lower rolling resistance is observed and vice versa. A change in speed does not result in an instant temperature change for the tyre matching the new speed, it is heating up or cooling down depending on if it is a speed increase or speed decrease. In [12] it is shown that a speed decrease from a certain speed at equilibrium temperature results in a temporary decrease in rolling resistance, after some time the temperature adjusts to the new speed and the rolling resistance increases. The same principle applies at a speed increase.

The brush model has been applied in many areas, in [4] and [2] the main focus is to capture the forces and moment acting on a tyre in motion at a constant speed.

An extended brush model is introduced to capture the behaviour more in detail. A single line brush model is switched out to a multi-line brush model. Each line contains n bristle elements, and each bristle element consists of three rubber elements, giving the output of forces and moment in all three directions. This leads to that the influence from camber angle, toe angle, and sideslip also can be accounted for and varied in the model. The developed extended brush model is calculated numerically and implemented in *MATLAB*. The result showed that the model had a good agreement in most ranges with the semi-empirical Magic Formula tyre model for longitudinal pure slip and lateral force. Also, comparisons to experimental data were carried out with good agreement in most ranges. The model parameters for the extended brush model were in both comparisons adjusted to get a good agreement meaning that no material tests nor measurements were carried out. This suggests that the brush model can be used to model acting forces and moments for a tyre with an agreement to reality if appropriate model parameters can be derived.

1.5 Outline

The chapters of the thesis are introduced and explained below:

Introduction - Contains the background to the problem and the related research. The research questions and approach are also presented.

Temperature measurements - The method used for gathering road temperature data is explained. The results from road measurements are also presented followed by a discussion.

Tyre model - Presents the tyre model.

Identification of model parameters - Two methods to determine the unknown model parameters are presented.

Results - The results from the identification of parameters as well as the results of the complete tyre model is presented.

Discussion - Discussion of the results.

Summary - Summary of the work carried out in the thesis, conclusions, and suggestions for future work.

2

Temperature Measurements

To examine what happens with the tyre temperature when driving in real driving conditions a collection of measurements was made. In this chapter, the test equipment is presented along with a description of how the measurements are collected. Finally, the results from the measurements are presented.

2.1 The car

The car used for collecting measurements was a Volvo XC60 diesel from 2017 with propulsion on the front wheels. In table 2.1 the weight distribution on the wheels is presented.

Table 2.1: *The weight distribution on the wheels with two passengers and measuring equipment.*

Wheel	Weight [kg]
Left front	597
Right front	585
Left rear	398
Right rear	410
Net weight	1830
Gross weight	1990

2.2 The tyre

One set of B-class all-season tyre was tested extensively. One set of A-class tyre was also tested, but on fewer occasions. Data of the tyres can be found in table 2.2.

Table 2.2: *Data of the tested tyres.*

Class	Rim size	Width	Aspect ratio	Load Index	Load class	Speed class
A	19	235	50	103	XL	H
B	19	235	50	103	XL	W

2.3 Measurement equipment

In this section the measurement equipment is presented.

2.3.1 Inner tyre sensor

The inner tyre sensor, the TTPMS sensor (Tyre Temperature and Pressure Monitoring System), was mounted inside the wheel by the valve. The TTPMS sensor sends out infrared light by 16 channels to measure the temperature across the width of the inner liner with an accuracy of ±1°C, see figures 2.1 and 2.2. It is also equipped with a pressure transducer with a ±10 *mBar* accuracy for gauge pressure measurement. The TTPMS sensor is wireless and sends temperature and pressure data to a receiver placed inside the car. Four TTPMS sensors were used for the measurements.

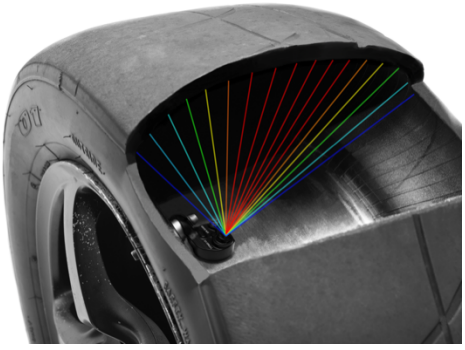

Figure 2.1: *Schematic figure of the TTMPS sensor [8].*

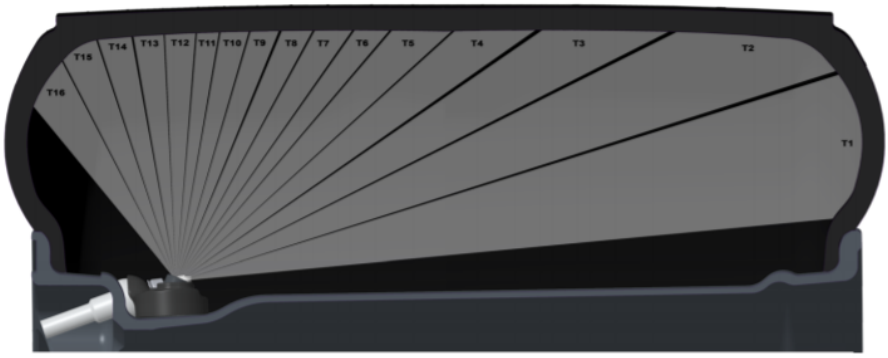

Figure 2.2: *Schematic figure of how the channels are distributed [8].*

2.3.2 Outer tyre sensor

The outer tyre sensor, the IRTS sensor (InfraRed Temperature Sensor), measure the temperature across the contact patch of the tyre with infrared light, see figure 2.3. The ten central channels measures with an accuracy of ±1°C while the first and last three channels measures with an accuracy of ±2°C in the temperature range 0 – 50°C.

The IRTS sensor was mounted under the car since the space inside the wheel-house of the car was insufficient, see figure 2.4. This meant that the IRTS sensor did not move with the suspension of the wheel resulting in a varying distance to the area of measurement. Only one IRTS sensor was at disposal which was placed by the left rear tyre.

Figure 2.3: *Schematic figure of the IRTS sensor [8].*

Figure 2.4: *Picture of the mounted IRTS sensor.*

2.3.3 Other measurement equipment

A mobile phone application was used to measure the speed and the road temperature was measured with a thermocouple. In the case of sunshine, the road temperature was measured in both shadow and sunlight. The wind speed and direction were collected from the Swedish Metrology and Hydrology Institute at the specific location while the outside temperature was measured with the temperature sensor installed in the car.

2.4 Collection of measurements

The collection of measurements was performed during spring 2021 in the area around Linköping in Sweden which allowed performing tests at a wide range of ambient conditions. A normal test day consisted of four different driving routes. One city route, one motorway route, one route at a large country road and one route at a small country road. The routes are explained in detail in section 2.5. Between each route, there was a pause for about 10-15 minutes to let the tyres cool down. Before the test day started the pressure of the tyres were regulated to 2800 *mBar* at the current outdoor ambient temperature. While driving, the speed and both inner- and outer tyre temperatures were recorded. Ambient conditions were also logged in connection with each route according to table 2.3. The weather was categorised into sunny, cloudy, rainy and snowy. The road condition was categorised into dry, damp and wet. Traffic conditions were only noted if there was something besides the ordinary (such as long queues on the motorway which influenced the speed).

Table 2.3: *Table explaining how the ambient conditions were logged.*

Conditions	Outside temperature	Road temperature	Wind	Weather	Road condition	Traffic conditions
Before driving	✓	✓	✓	✓		
During driving	✓			✓	✓	✓
After driving	✓	✓	✓	✓		

2.5 Driving routes

The driving routes are explained in each subsection. Data of the banking was available for the motorway and a majority of the large country road[17]. The database in which the banking was available is controlled and handled by the organisation that handle the Swedish roads called Trafikverket. The influence of banking on the tyres is discussed in section 2.7.

2.5.1 City

The city route consisted of roads with low-speed limits, 30-40 km/h, traffic lights, intersections and traffic heavily influenced driving. A map with the city route marked is shown in figure 2.5. The city route was driven two laps counterclockwise without a pause. Start and finish point were at Vallarondellen. The speed held during the city route varied, adapting to traffic and speed limits.

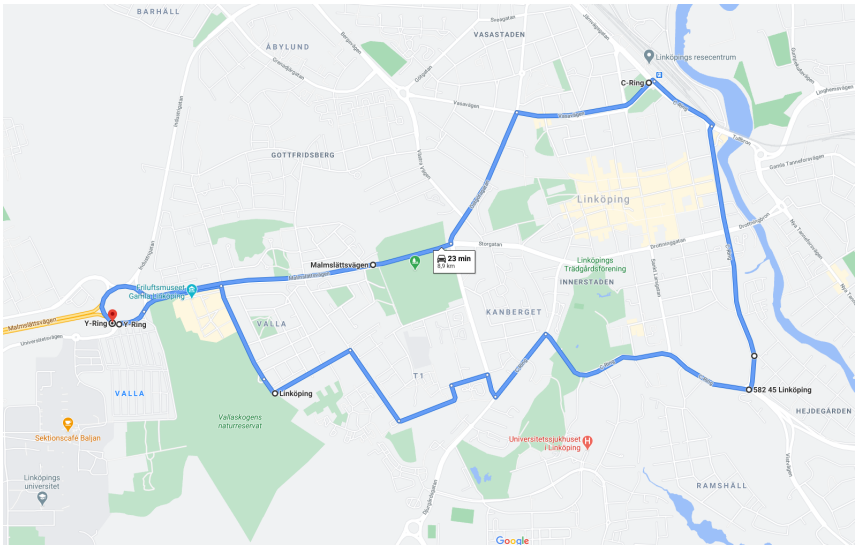

Figure 2.5: *The city driving route.*

2.5.2 Motorway

The motorway was a four-lane road (two lanes in each direction) with speed limits of 110-120 km/h, a consistent speed of 110 km/h was the aim but adaptation to traffic required lower speeds at some instances. A map with the motorway route marked is shown in figure 2.6. The starting point was Linköping, then Mantorp and it finished outside Norrköping. Banking of the road can be seen in figure 2.7.

Figure 2.6: *The motorway driving route.*

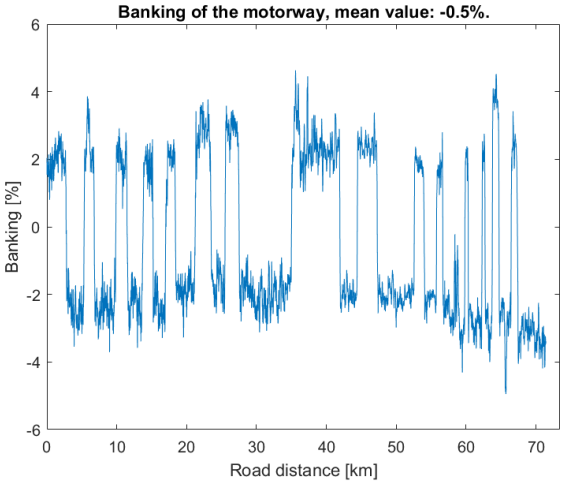

Figure 2.7: *The banking of the motorway.*

2.5.3 Large country road

The large country road consisted of a two-lane road (one lane in each direction). Speed limits varied between 40-80 km/h, a large portion of the road had the speed limit of 80 km/h but the speed limit was lowered when driving through communities. A speed of 80 km/h was the aim but speed limits and traffic required lower speeds in some instances. A map with the large country route marked is shown in figure 2.8. The starting point was Söderköping and the finish point was outside Finspång. Banking of the road can be seen in figure 2.9.

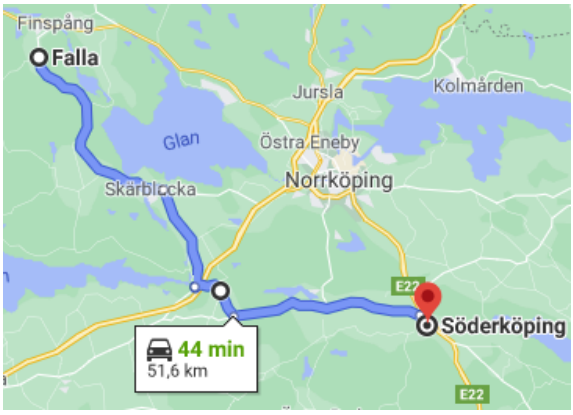

Figure 2.8: *The large country driving route.*

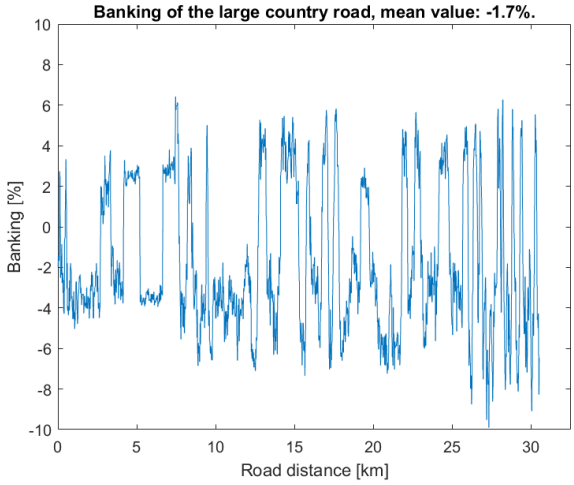

Figure 2.9: *The banking of the large country road.*

2.5.4 Small country road

The small country road consisted of one lane shared by each direction in the beginning. At the end of the route, the road had two lanes (one lane in each direction). The route was curvy in the beginning but became more straight at the end. The speed limit varied between 50-70 km/h. A speed of 50 km/h was the aim but at the beginning of the route it varied a lot since adaptation to curves was required. At the end of the route a more consistent speed of 50 km/h was possible. A map with the route marked is shown in figure 2.10. The starting point was outside Finspång and the finish point was just north of the lake Roxen.

Figure 2.10: *The smaller country driving route.*

2.6 Results

In this section measurements from each route of a complete test day is first presented followed by collocation of all measurements.

2.6.1 Measurements from a test day

The figures 2.11-2.14 illustrates measurements of the inner-, outer temperature and speed for the B-class tyres during a full test day. The conditions that the tests were run in are presented in table 2.4 - 2.7, test numbers 4, 11, 15, 18. The temperature, both the inner- and outer sensor value, have been filtered by using a moving average. The moving average takes the average of the temperature 15 seconds forward in time and 15 seconds back in time for each data point. There are 16 channels measuring temperature in the sensor, the temperature displayed is the mean value of channel 6-10. A plot of all channels for the measurement displayed in figure 2.12 is shown in figure 2.15. The spread of temperature between channels differs for each sensor but channel 6-10 is in the middle segment for all sensors. The phone app recording speed records the average speed per one kilometre, in the plot the speed is therefore updated with a one-kilometre interval.

The vertical dashed line in the plots shows when the equilibrium point is assumed to be reached for each route. At high speeds, the inner tyre temperature is warmer compared to lower speeds at similar conditions due to a higher rate of deformation. A change in speed at high speed leads to an almost instant change in temperature, see figure 2.12 at 10 to 15 minutes. This behaviour is not seen as clearly for lower speeds, figure 2.11, it might be due to that there is less difference between inner tyre temperature and ambient temperature or that the change in speed is not as big. The equilibrium temperature is estimated over a period to lower the influence of speed changes. The time of the routes differs, the small country road has a duration of 35 minutes compared to the other routes of 40-45 minutes. For the small country road the equilibrium point was set to occur after 25 minutes, it can be seen in figure 2.14 that the temperature has stabilised by then. For the city, motorway, and large country road the equilibrium point was set to occur after 30 minutes.

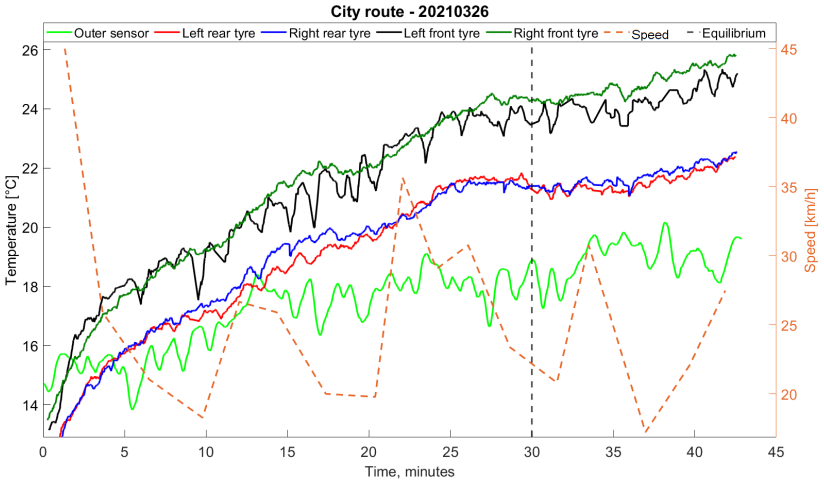

Figure 2.11: *Test number 4. The temperature measurement for the city route collected 2021-03-26. Ambient temperature:* 12°C. *Road temperature:* 13°C.

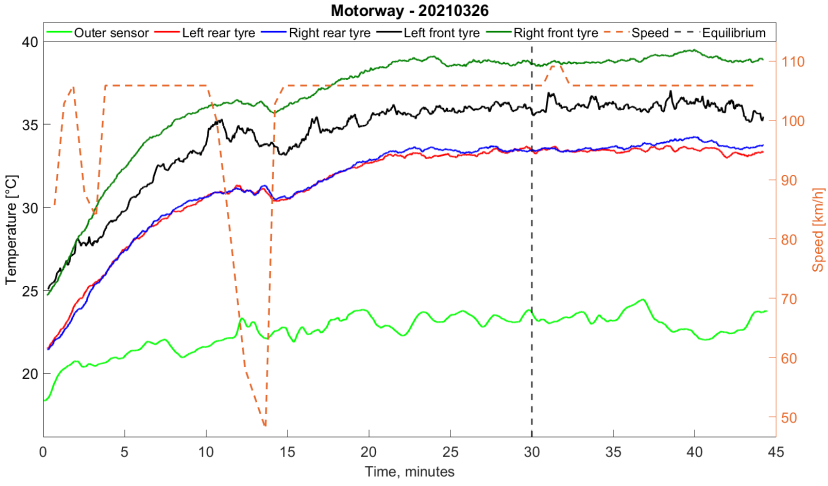

Figure 2.12: *Test number 11. The temperature measurement for the motorway route collected 2021-03-26. Ambient temperature:* 13°C. *Road temperature:* 14°C.

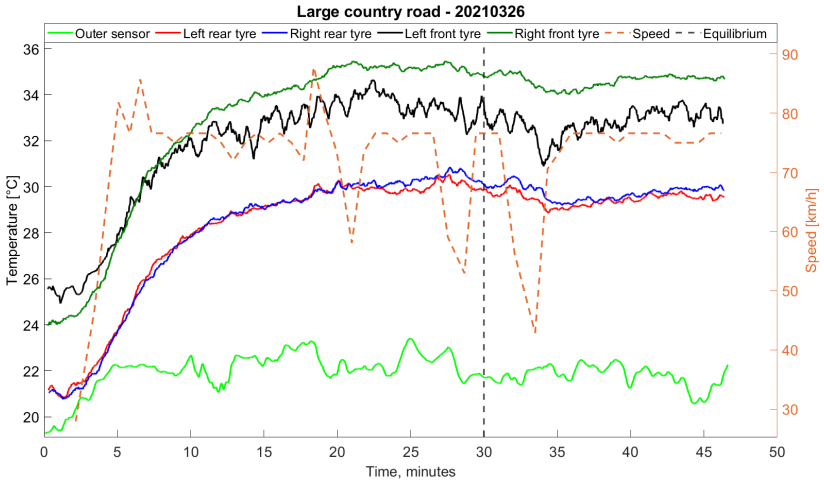

Figure 2.13: *Test number 15. The temperature measurement for the large country road route collected 2021-03-26. Ambient temperature:* 13°C. *Road temperature:* 13°C.

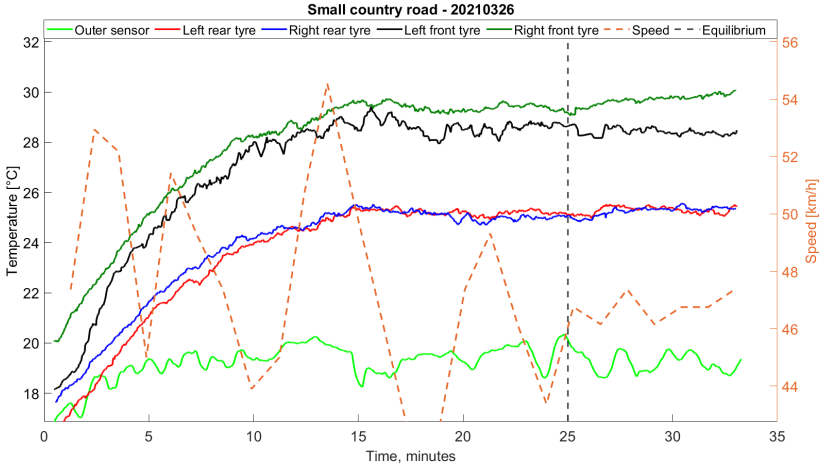

Figure 2.14: *Test number 18. The temperature measurement for the small country road route collected 2021-03-26. Ambient temperature:* 12°C. *Road temperature:* 12°C.

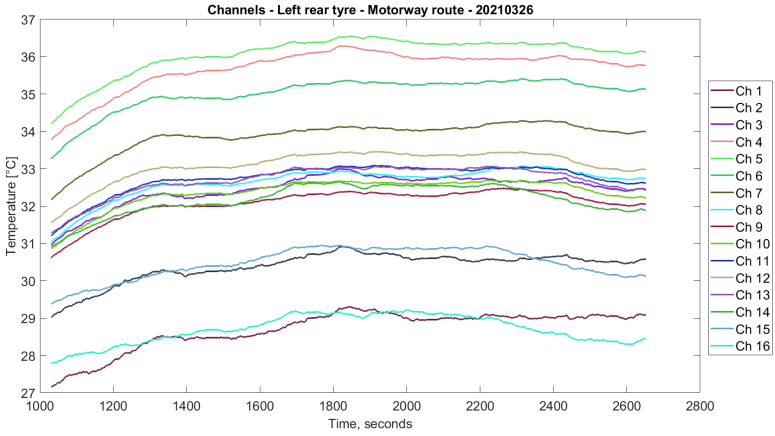

Figure 2.15: *The 16-channels for the left rear tyre for test number 11.*

2.6.2 Collocation of measurements

In table 2.4 - 2.7 a summary of all test days are presented, each test has been given a number. When the weather was sunny the road temperature differed in the sun and shadow, in the tables an average of the two temperatures was used. The inner tyre temperature is the mean temperature of channel 6-10 for the rear wheels after equilibrium. The outer tyre temperature is the mean temperature of channel 6-10 for the outer sensor after equilibrium. Four measurements numbered 5, 6, 7 and 12 were performed at a lower initial pressure.

In the tables the following abbreviations are used: Nr - Test number, Amb. T [°C] - the ambient temperature, Road T [°C]- the road temperature, R. cond. - the road condition, Wind - wind speed $[m/s]$ and direction, Inner T [°C] - the average inner tyre temperature, Outer T [°C] - the average outer tyre temperature, v - the average speed $[km/h]$, P $[mBar]$- the average pressure.

Table 2.4: *Collocation of city measurements.*

Route	City						
Nr	1	2	3	4	19	20	21
Tyre class	B	B	B	B	A	A	A
Amb.T	4	7	10	12	7	11	20
Road T	7	8	12	13	10	12	19
Weather	Cloudy	Sunny/cloudy	Sunny	Sunny	Cloudy	Sunny/cloudy	Sunny
R. cond.	Wet	Dry	Dry	Dry	Dry	Dry	Dry
Wind	5 - SW	1 - NW	3 - N	5 - S	2 - S	3 - E	5 - W
Inner T	11.3	17.1	19.5	21.7	15.8	17.9	25.8
Outer T	6.9	14.5	17.0	19.1	14.7	17.3	25.1
v	27	25	26	26	27	25	26
P	2779	2903	2930	2917	2900	2903	2910

Table 2.5: *Collocation of motorway measurements.*

Route	Motorway									
Nr	5	6	7	8	9	10	11	22	23	24
Tyre class	B	B	B	B	B	B	B	A	A	A
Amb.T	1	1	2	5	7	8	13	8	10	20
Road T	3	4	1	8	11	7	14	13	16	22
Weather	Cloudy	Snow	Snow/rain	Cloudy	Sunny	Cloudy	Sunny	Cloudy	Sunny	Sunny
R. cond.	Dry	Damp	Wet	Dry	Dry	Dry	Dry	Dry	Dry	Dry
Wind	3 - E	5 - W	6 - SW	5 - SW	3 - N	8 - W	4 - SW	1 - W	2 - NE	4 - W
Inner T	22.2	21.8	18.9	27.1	29.5	28.8	33.6	25.3	27.3	35.9
Outer T	0.3	4.8	2.6	6.0	19.3	20	23.1	17.6	20.5	28.7
v	103	104	103	104	104	105	103	103	104	104
P	2706	2732	2364	2901	2984	2900	2999	2954	2960	2969

Table 2.6: *Collocation of measurements from the large country road.*

Route	Large country road						
Nr	12	13	14	15	25	26	27
Tyre class	B	B	B	B	A	A	A
Amb.T	1	6	6	13	9	10	24
Road T	4	8	10	13	15	15	27
Weather	Cloudy	Sunny	Cloudy	Sunny/cloudy	Cloudy	Cloudy	Sunny
R. cond.	Damp	Dry	Damp	Dry	Dry	Dry	Dry
Wind	4 - W	3 - N	4 - SW	3 - SW	2 - NW	2 - SE	3 - NW
Inner T	18.5	23.6	22.2	29.6	21.9	24.6	34.5
Outer T	3.4	15.9	9.6	21.8	17.5	20.9	31.1
v	70	68	73	73	72	72	72
P	2710	2938	2866	2981	2943	2952	2986

Table 2.7: *Collocation of measurements from the small country road.*

Route	Small country road					
Nr	16	17	18	28	29	30
Tyre class	B	B	B	A	A	A
Amb.T	5	6	12	10	10	24
Road T	6	10	12	15	15	26
Weather	Sunny	Cloudy	Cloudy	Cloudy	Cloudy	Sunny
R. cond.	Dry	Damp	Dry	Dry	Dry	Dry
Wind	2 - N	5 - W	4 - SW	2 - SW	1 - SW	3 - NW
Inner T	19.7	16.7	25.3	21.3	21.9	34.9
Outer T	11.9	5.4	19.0	18.0	18.2	32.0
v	45	46	47	47	46	45
P	2907	2827	2950	2957	2958	3016

2.7 Discussion

There is a difference in temperature between the front wheels and the rear wheels, as can be seen from the results in section 2.6, . This is due to the front wheel propulsion of the car. When torque is applied at a wheel the rolling resistance increases which give an increase in temperature [18]. There is also a difference between the two front wheels. Figure 2.7 and 2.9 show the banking of the motorway and the large country route. The front wheels have a toe in angle of 1° and the road is tilted to the right. To keep the vehicle going straight a constant small steering angle to the left is required. The right front tyre will in this case have a larger side slip angle than the left front wheel which result in higher rolling resistance and higher temperature [16]. Figure 2.16 and 2.17 show two temperature measurements performed at the smaller country road. The measurement correlating to figure 2.16 was executed while driving on the right side of the road. Figure 2.17 correlates to a measurement when driving as much as possible on the left side of the road. The difference between the two measurements corresponds with the reasoning behind the difference in temperature between the front wheels. It is also possible that a part of the temperature increase comes from the engine because a heat outlet from the engine was directed to the right side of the vehicle on the car that was used. Measurements at standstill with the engine running did not indicate that the right front tyre became warmer. At higher speeds more cooling of the engine is required which could influence the temperature to a larger extent.

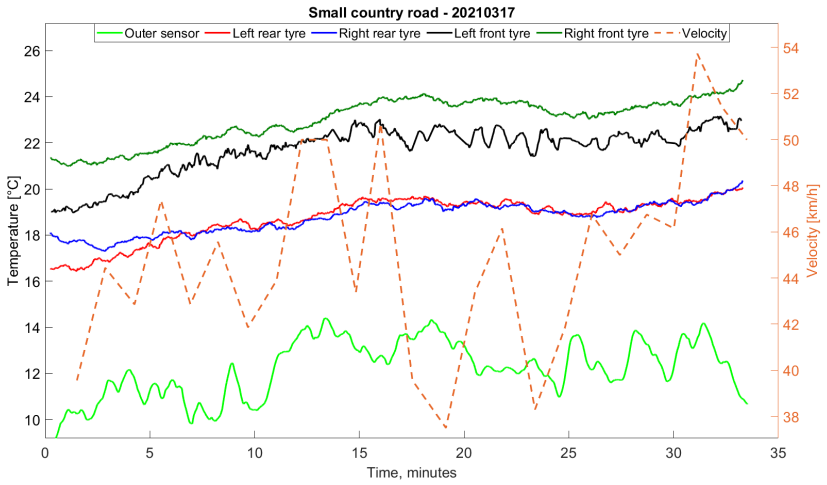

Figure 2.16: *Temperature measurement from the small country road while driving on the right side.*

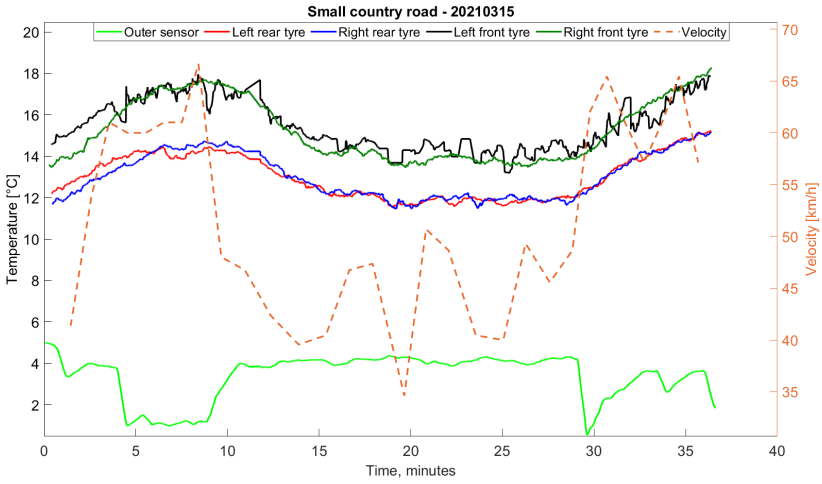

Figure 2.17: *Temperature measurement from the small country road while driving on the left side.*

The road temperature measurement which is displayed in table 2.4-2.7 indicate that the road was warmer than the ambient temperature. It is important to note that it could be influenced by error in the measuring equipment.

The road condition influences the outer tyre temperature as can be seen in test number 13 and 14 which had the same ambient temperature but different road conditions. That resulted in different outer tyre temperatures, the test at dry condition gave 6.3 °C higher temperature. One can also observe contradicting results for the road conditions influence on the outer tyre temperature by comparing test number 5 and 6. Test number 5 had dry conditions and test number 6 had damp conditions. The outer tyre temperature was in this case 4.5 °C higher for the damp condition compared to the dry condition. It could however be caused by the influence of the wind. During the motorway route, the driving direction is mostly towards east. For test number 5 the wind direction was from east and for test number 6 from west.

There is a lot of different conditions that could influence the inner tyre temperature, it is therefore hard to test the repeatability. However, test number 28 and 29 were run in similar conditions and gave similar results which gave some indication of repeatability. Trying to identify how each condition influences the tyre would require more extensive testing. From these tests a clear connection between ambient temperature, road temperature, speed and inner tyre temperature can be seen. According to [19] the ambient temperature influences the internal average temperature by +1 ~2 °C for an increase of +10°C while the road temperature influence the internal average temperature by +6~7°C for an increase of +10°C. Higher speeds, road- and ambient temperatures generate higher inner tyre temperature.

Three full test days were carried out with the A-tyres and some differences can be seen between the two classes. For rather similar conditions the B-tyres reached a higher temperature in the city driving, compare test number 2 and 3 for the B-tyres with test number 19 and 20 for the A-tyres. More extensive testing is however required to conclude the impact of tyre class.

3
Tyre model

A lot of different models are available for tyres. These models have different purposes and have different advantages and drawbacks. Making a model for rolling resistance with temperature dependence can be done in different ways. Finite element models require material testing and a lot of computational power which make them difficult to implement in real-time vehicle dynamic simulations. The magic formula for tyres is based on empirical data and does not model rolling resistance which is the scope of this thesis. There are also simpler analytical models available for the rolling resistance and its dependence on temperature [12][9].

The extended brush model presented in [4] gives a representation of how the tyre interacts with the road and the forces that occur. The extended brush model requires little computational power and can derive the rolling resistance. In this thesis, a simplification of the extended brush model has been chosen as a base for continuous work.

3.1 Tyre

In figure 3.1 a tyre with different radii and forces is pictured. The effective rolling radius is somewhere in between these two different radii $R_l < R_e < R_u$. According to SAE J670e (1976) the effective rolling radius is the ratio of the linear velocity of the wheel centre in the x-direction to the angular velocity [13]. Since the angular velocity is unknown another expression of the effective rolling radius is used. The effective rolling radius is defined as the distance from the centre of the wheel to a point in the middle of the centre contact patch and the edge of the contact patch as shown in figure 3.1 in accordance with [10]. Equation 3.1 give the effective rolling radius expressed with loaded and unloaded tyre radius. The force F_z is

offset by a distance e from the centreline of the wheel, which is the cause for the rolling resistance moment.

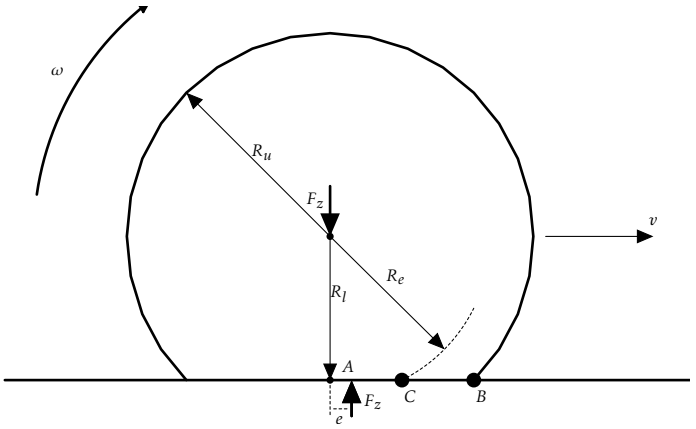

Figure 3.1: *Definition of tyre radius.*

$$R_e = \sqrt{\frac{R_u^2 + 3R_l^2}{4}} \tag{3.1}$$

3.2 The brush model

The concept of the brush model is to split up the tyre into bristles. Bristles are equally divided over a segment angle θ, see figure 3.2. In this work, one line of bristles was used which is sufficient when only vertical forces are of interest. The bristles are placed on a stiff carcass. Deformations and forces can be calculated individually for all bristles, how the forces are modelled is explained in detail in section 3.3. Increasing the number of bristles give an increase in accuracy but also increases the computational effort. The summation of all forces in the bristles gives the total force acting on the tyre. The total moment is given by taking the sum of all bristle's contribution to the moment. In equation 3.3, $F_{b,i}$ is the vertical force from bristle i and Δx_i is the distance to that bristle from the centre of tyre contact. It has a positive value if it is behind the centre of the wheel and a negative value if it is in front of the centre of the wheel.

$$F_z = \sum_i^n F_{b,i} \tag{3.2}$$

$$RRM = \sum_i^n F_{b,i} \Delta x_i \tag{3.3}$$

Only a small part of the circumference of the tyre is in contact with the road, that is the region of interest since that is where the forces appear. The segment angle must capture all the bristles which are in contact with the road. The segment angle was set to, $\theta = \pi/2$. A tyre with substantively low stiffness could require an increased segment angle. Equation 3.4 shows how the position of each bristle, index i, is updated when the tyre is rolling. This ensures that the bristles are always kept within the segment angle.

$$\varphi_i^{t+\tau} = \begin{cases} \varphi_i^t - \omega\ \tau, & |\varphi_i^{t+\tau}| \leq \frac{\theta}{2} \\ \varphi_i^t - \omega\ \tau - \theta\ sgn(\varphi_i^{t+\tau}), & \text{otherwise} \end{cases} \tag{3.4}$$

Where ω for a set velocity is defined as:

$$\omega = \frac{v}{R_e} \tag{3.5}$$

When the bristle position is known the deformation of each bristle can be calculated as:

$$\delta_i = \begin{cases} -R_l + R_u \cdot cos(\varphi_i), & -R_l + R_u \cdot cos(\varphi_i) \geq 0 \\ 0, & \text{otherwise} \end{cases} \tag{3.6}$$

The conditions of δ_i bigger than zero is necessary since bristles within the segment angle but not in contact with the road otherwise would give negative values which is not the case.

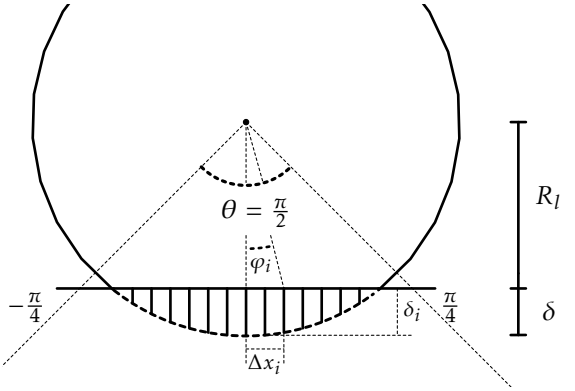

Figure 3.2: *Illustration of bristles and segment angle.*

3.3 Bristle model

Each bristle is representing one small part of the tyre and the bristle model is the correlation between the deformation this part is exposed to and the force. The main characteristics the bristle model captures are the rubber characteristics of the tyre but it also takes the tyre as a whole into account. Because of the molecular bindings within the rubber, it shows both frequency dependent and frequency independent features. Each bristle therefore consists of a viscoelastic model in parallel with an internal friction model. The viscoelastic part captures the frequency dependent features while the frequency independent features are captured by the internal friction element. In total the force becomes:

$$F_b = F_{ve} + F_f \tag{3.7}$$

3.3.1 Viscoelastic model

The Zener model is used to represent the viscoelastic characteristics and can be seen in figure 3.3. It consists of a spring in parallel with a spring in series with a damper. Important relations of the model are displayed in equation 3.8 - 3.13. Here the force from the damper is denoted F_c and the force from the spring attached to the damper is denoted F_{k_1}, the deformation of the damper is denoted δ_c and the deformation of the spring attached to the damper is denoted δ_{k_1}. The total deformation of the viscous part is denoted δ_v and the total deformation of the elastic part is denoted δ_e.

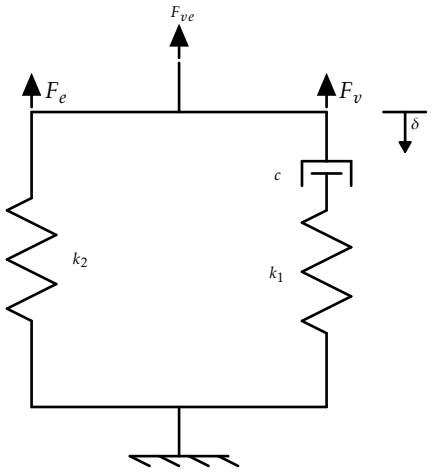

Figure 3.3: *Viscoelastic model.*

$$F_{ve}(t) = F_e(t) + F_v(t) \tag{3.8}$$

$$F_c(t) = F_{k_1}(t) = F_v(t) \tag{3.9}$$

$$F_{k_1}(t) = k_1 \delta_{k_1}(t) \tag{3.10}$$

$$F_c(t) = c\ \dot{\delta}_c(t) \tag{3.11}$$

$$F_e(t) = k_2 \delta(t) \tag{3.12}$$

$$\delta_c(t) + \delta_{k_1}(t) = \delta_v(t) = \delta_e(t) = \delta(t) \tag{3.13}$$

From equation 3.8 - 3.13 an expression in the time domain was derived. The complete solution is presented in appendix A.

$$\dot{F}_{ve}(t, \delta) = -\frac{k_1}{c}\ F_{ve}(t) + \frac{k_1 k_2}{c}\ \delta(t) + (k_1 + k_2)\ \dot{\delta}(t) \tag{3.14}$$

In the frequency domain the equation looks the following way:

$$\frac{F_{ve}(s)}{\delta(s)} = \frac{c\ (1 + \frac{k_2}{k_1}) \cdot s + k_2}{\frac{c}{k_1} \cdot s + 1} \tag{3.15}$$

Figure 3.4 shows a bode diagram of the viscoelastic model with different values set for the variables presented in table 3.1. A change of the constant c influence at what frequency the phase shift occurs and a change in k_1 influence both the frequency of the phase shift as well as the magnitude of the frequency response after the phase shift which is seen in figure 3.4. A change of variable k_2 influences the magnitude of the frequency response. The deformation responsible for rolling resistance occurs at 10-150 Hz [1]. The initial stiffness of the tyre is set by k_2. The stiffness of the tyre will be increased at a frequency decided by the parameter c, the increase at this frequency is influenced by the parameter k_1. Increased rolling resistance will occur at the frequencies where the phase shift occurs. The increase of rolling resistance at this frequency is influenced by the parameter k_1.

Table 3.1: *Values of variables used in figure 3.4.*

Case	k_1	k_2	c
1	100	3300	0.32
2	100	3300	3.2
3	150	3300	0.32
4	100	3000	0.32

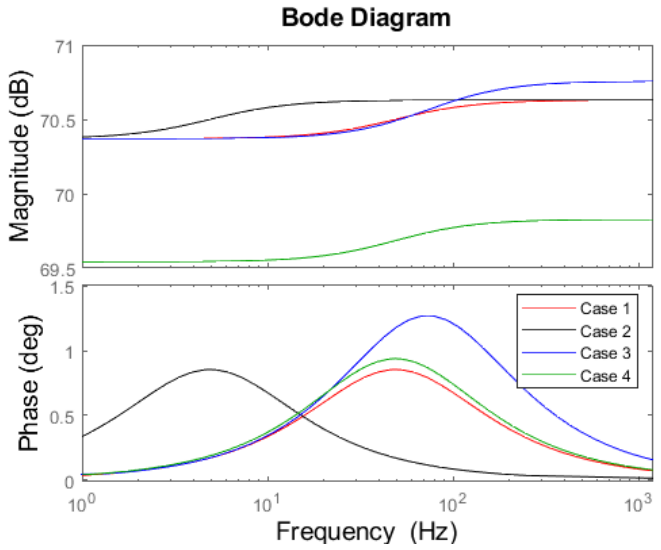

Figure 3.4: *Bode diagram of the viscoelastic model with different values for the variables.*

In order to implement equation 3.14 numerically the Crank-Nicolson method [3] was used. The function f was defined as:

$$\dot{F}_{ve}(t, \delta) = f(t, F_{ve}, \delta) \tag{3.16}$$

In each time interval, τ, the viscoelastic force is approximated using:

$$F_{ve}^{t+\tau} \approx \frac{1}{2}(f^{t+\tau}(t, F_{ve}, \delta) + f^{t}(t, F_{ve}, \delta)) \cdot \tau + F_{ve}^{t} \tag{3.17}$$

The deformation was approximated using first-order Euler method:

$$\dot{\delta}^{t+\tau} \approx \frac{\delta^{t+\tau} - \delta^{t}}{\tau} \tag{3.18}$$

$$\dot{\delta}^{t} \approx \frac{\delta^{t} - \delta^{t-\tau}}{\tau} \tag{3.19}$$

The resulting equation of the force becomes:

$$F_{ve}^{t+\tau} = \frac{(2c - k_1\tau) \cdot F_{ve}^{t} + (k_1 k_2 \tau + c(k_1 + k_2)) \cdot \delta^{t+\tau} + (\tau k_1 k_2)\delta^{t} - c(k_1 + k_2) \cdot \delta^{t-\tau}}{(2c + k_1\tau)} \tag{3.20}$$

It is also possible to derive an analytical expression of the model which is explained in section 3.4.

3.3.2 Internal friction model

To describe the internal friction and the Payne effect, also known as the Fletcher-Gent effect, a Masing model was used. In tyres the Payne effect describes the stress-strain behaviour of the rubber which contains fillers of carbon black. The Masing model consists of several parallel Jenkins elements. The Jenkin element consists of a spring in series with a Coulomb friction element. The Masing model with five Jenkins elements is shown in figure 3.5 and a plot of the resulting force with applied deformation is shown in figure 3.6. In the plot a sinusoidal deformation is applied with varying amplitudes. Increasing the number of Jenkin elements increase the computational effort but will also provide a smoother curve.

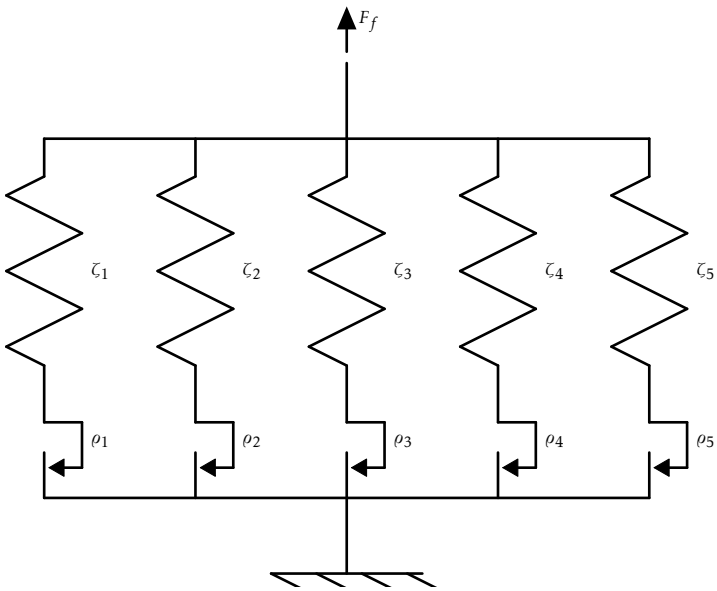

Figure 3.5: *The Masing model with five Jenkins element.*

Table 3.2: *Parameters used in figure 3.6*

ρ_1	ρ_2	ρ_3	ρ_4	ρ_5	ζ_1	ζ_2	ζ_3	ζ_4	ζ_5
0.2	0.4	0.6	0.8	1.2	1200	1000	800	600	400

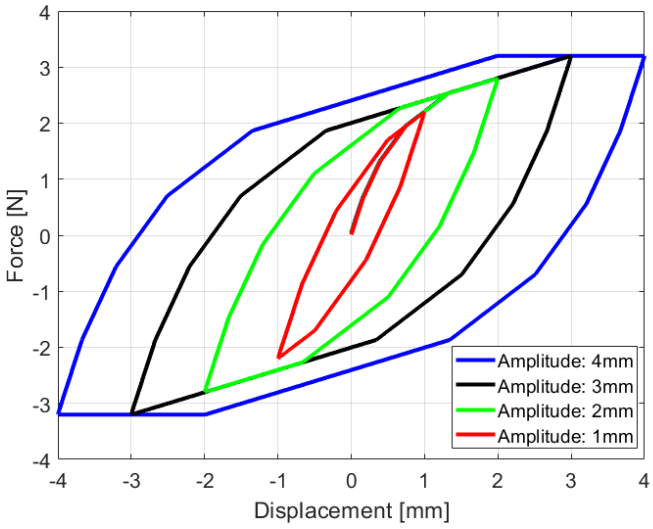

Figure 3.6: *A plot showing the corresponding force when the deformation is applied as a sinus curve at different amplitudes. Values of the parameters is presented in table 3.2.*

The equation for the Masing model is shown below, where j is the number of Jenkin elements.

$$F_f(\delta) = \sum_{i=1}^{j} F_{f,i}(\delta) \tag{3.21}$$

$F_{f,i}$ is the force in each Jenkin element which is governed by the following equation:

$$\dot{F}_{f,i} = \begin{cases} \zeta_i \dot{\delta}, & |F_{f,i}| < \rho_i \text{ or } (|F_{f,i}| = \rho_i \text{ and } sgn(\dot{\delta} \cdot F_{f,i}) \leq 0) \\ 0, & \text{otherwise} \end{cases} \tag{3.22}$$

The parameter ζ_i is the stiffness of the spring in the Jenkin element and the parameter ρ_i is the value of the Coulomb friction element in the Jenkin element. The Coulomb friction element defines a maximum force for the Jenkin element.

To calculate the force from the Jenkin element a test force is first calculated. The test force is the force of the Jenkin element without the Coulomb friction element. If the test force is within the maximum force defined by the Coulomb friction element the value is accepted, otherwise it is changed to $\pm\rho_i$. The sign of the force is still kept, the force from the Jenkin element will therefore be kept within the limit $-\rho_i \leq F_{f,i} \leq \rho_i$.

The test force, $\tilde{F}^t_{f,i}$, is calculated by:

$$\tilde{F}^t_{f,i} = F^{t-\tau}_{f,i} + \zeta_i \Delta\delta \tag{3.23}$$

where $\Delta\delta$ is given by:

$$\Delta\delta = \delta^{t+\tau} - \delta^t \tag{3.24}$$

The resulting equation for the force from one Jenkin element becomes:

$$F^t_{f,i} = \left((|\tilde{F}^t_{f,i}| > \rho_i) \cdot sgn(\tilde{F}^t_{f,i})\right) \cdot \rho_i + \left(|\tilde{F}^t_{f,i}| \leq \rho_i\right) \cdot \tilde{F}^t_{f,i} \tag{3.25}$$

By increasing the number of Jenkin elements, the Payne effect can be modelled more accurate which is important at small deformations. Since the tyre deformation is large at each revolution capturing this effect is not of great importance. The change of rolling resistance is not influenced a lot by changing the amount of Jenkin elements which can be seen in figure 3.7. In figure 3.7 the force applied to the tyre from the internal friction is displayed, the tyre is rolling to the right, the beginning of the contact patch is around bristle number 130. For each Jenkin element two model parameters are added which complicates the process of finding model parameters. Therefore, the internal friction part is modelled with a single Jenkin element.

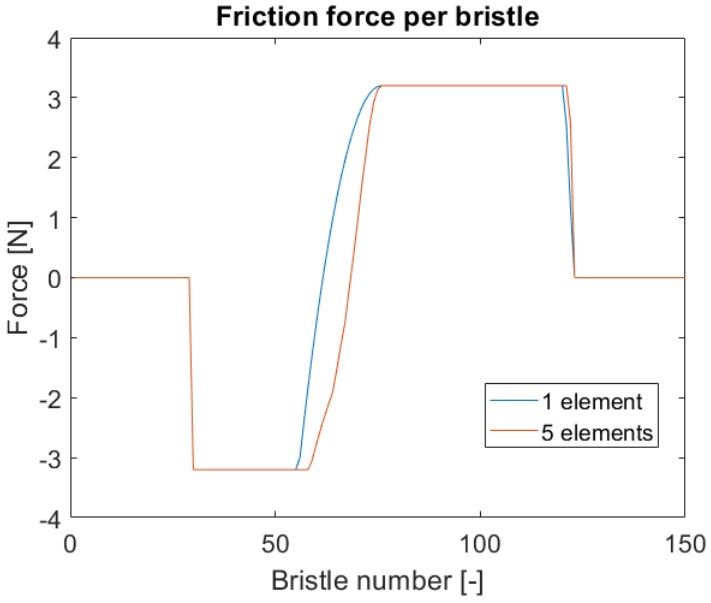

Figure 3.7: *A plot showing the influence of the amount of Jenkin elements to the friction force.*

3.3.3 The complete bristle model

The final bristle model is shown in figure 3.8. Figure 3.9 shows the relation between deformation and force at two different frequencies with the parameters according to table 3.3. In total five parameters needs to be decided. The model show hysteresis, the area within the plots in figure 3.9 is the energy that will be dissipated. At higher frequency more energy will be dissipated which result in higher rolling resistance.

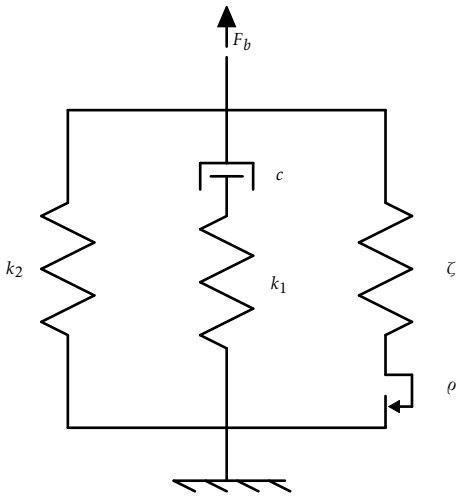

Figure 3.8: *Complete bristle model.*

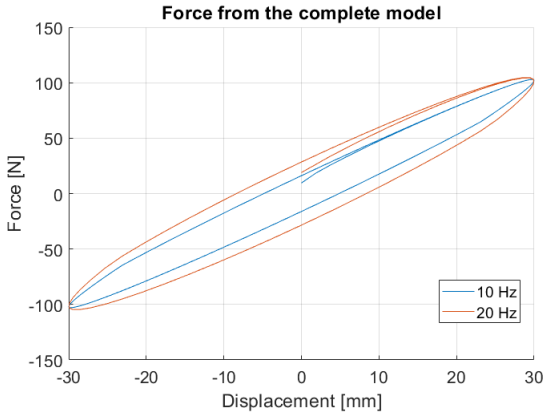

Figure 3.9: *Plot showing the deformation and corresponding force for the complete bristle model at two different frequencies.*

Table 3.3: *Parameters used in figure 3.9*

k_1	k_2	c	ζ	ρ
100	3300	0.32	800	3.2

3.3.4 Outline of code

There are two different options available in the model, either a load can be set or a loaded tyre radius. The outline of the code is shown in figure 3.10, the iteration displayed in the red box is only used if a load is set as an input. First speed, simulation time, step time (τ), segment angle, tyre parameters and number of bristles are set. An initial loaded tyre radius is set and a load (optional). This is followed by the calculation of bristles, deformation, and forces. The forces of the viscoelastic part can be calculated in two different ways, either by the analytical model or by the bristle model. The analytical model was only used when trying to identify parameters with the divided model method, explained in section 4.2.2. These steps had to be repeated until convergence, the forces are set to zero in each bristle from the beginning and since the force is dependent on previous forces this loop had to be iterated. If the load was set as an input and there was a difference between the tyre force in the z-direction and the load, the loaded tyre radius needs to be updated. This is done until convergence is reached. When identifying the parameters, the loaded tyre radius and the load were already known. The iterations for updating tyre position were therefore not used.

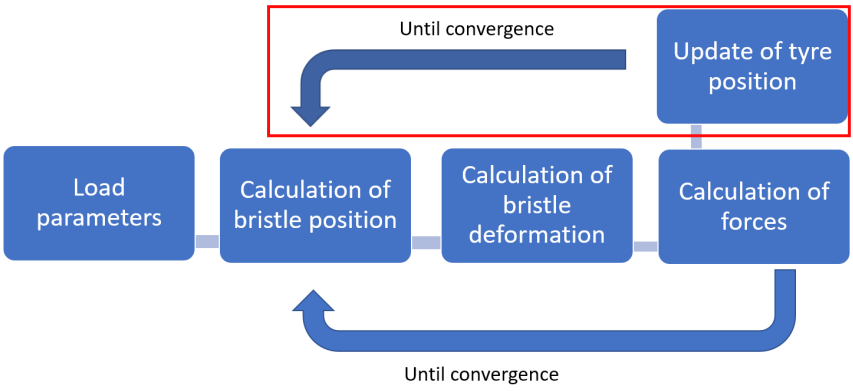

Figure 3.10: *Outline of the code.*

3.4 Analytical model

It was possible to derive an analytical solution for the viscoelastic part. The analytical model is displayed in figure 3.11. Equation 3.26 and 3.27 describe the force and corresponding δ_{k_1} and δ positions.

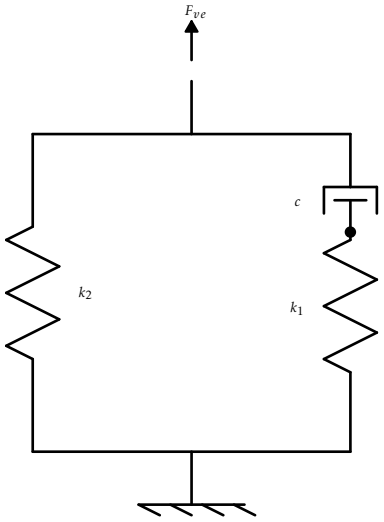

Figure 3.11: *Model used for analytical solution.*

$$\uparrow F_{ve} - k_1 \delta_{k_1} - k_2 \delta = 0 \tag{3.26}$$

$$\uparrow k_1 \delta_{k_1} - c\,(\dot{\delta} - \dot{\delta}_{k_1}) = 0 \tag{3.27}$$

These equations gave an expression of how the force F_{ve} and position δ_{k_1} and δ varied over time:

$$F_{ve}(t) = k_1 \delta_{k_1}(t) + k_2 \delta(t) \tag{3.28}$$

$$\dot{\delta}_{k_1}(t) + \frac{k_1}{c} \delta_{k_1}(t) = \dot{\delta}(t) \tag{3.29}$$

Equation 3.28 and 3.29 can be expressed with φ instead of t, $\varphi(t)$ is given by the following expression:

$$\varphi(t) = \varphi_1 - \omega t \tag{3.30}$$

The angle φ_1 can be derived from the loaded and unloaded tyre radius:

$$\varphi_1 = \arccos\left(\frac{R_l}{R_u}\right) \tag{3.31}$$

A description of the angle φ is given in figure 3.12. φ_1 is the angle to the point where the tyre first meets the road. φ_2 is the angle to the point where the force f_z is equal to zero, with the constraint that the angle is less than φ_1. φ_2 is not shown in the figure since it varies depending on load cases and tyre parameters. With this model the force is not zero at the end of the contact patch, it becomes zero before the end of the contact patch. This is caused by the simplifications made to model the hysteresis of the tyre and is not the case in reality.

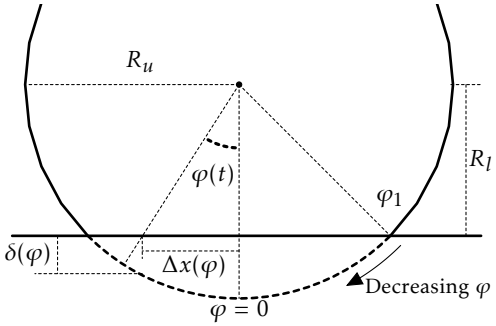

Figure 3.12: *Illustrating figure of φ and Δx.*

An expression for how δ, $\dot{\delta}$ and $\dot{\delta}_{k_1}$ varies with φ is given by:

$$\delta(\varphi) = R_u cos(\varphi) - R_l \tag{3.32}$$

$$\dot{\delta}(t) = \frac{d\delta}{dt} = \frac{d\delta}{d\varphi}\frac{d\varphi}{dt} = -\omega\delta'(\varphi) = \omega R_u sin(\varphi) \tag{3.33}$$

$$\dot{\delta}_{k_1}(t) = \frac{d\delta_{k_1}}{dt} = \frac{d\delta_{k_1}}{d\varphi}\frac{d\varphi}{dt} = -\omega\delta'_{k_1}(\varphi) \tag{3.34}$$

By inserting equation 3.33 and 3.34 into equation 3.29 a differential equation for $\delta_{k_1}(\varphi)$ was obtained:

$$-\omega\delta'_{k_1}(\varphi) + \frac{k_1}{c}\delta_{k_1}(\varphi) = \omega R_u sin(\varphi) \tag{3.35}$$

Solving the differential equation results in the following expression for $\delta_{k_1}(\varphi)$. The solution of the differential equation is presented in appendix B.

$$\delta_{k_1}(\varphi) = \frac{c\ \omega\ R_u\ (c\ \omega\ \cos(\varphi) + k_1\ \sin(\varphi))}{c^2\omega^2 + k_1^2} + C_1 e^{\frac{k_1\varphi}{c\,\omega}} \tag{3.36}$$

The arbitrary constant can be derived from the condition that there is no deformation just as the contact patch is entered, $\delta_{k_1}(\varphi_1) = 0$, see figure 3.12.

$$C_1 = -\frac{c\ \omega\ R_u e^{-\frac{k_1 \varphi_1}{c\ \omega}}\ (c\ \omega\ \cos(\varphi_1) + k_1 \sin(\varphi_1))}{c^2\omega^2 + k_1^2} \tag{3.37}$$

Inserting equation 3.36, 3.37 and 3.32 to equation 3.28 results in the following expression for the viscoelastic force:

$$\begin{aligned} F_{ve}(\varphi) = k_1 & \frac{(c\ \omega\ R_u\ (c\ \omega\ \cos(\varphi) + k_1 \sin(\varphi)))}{c^2\omega^2 + k_1^2} - \\ & k_1 \frac{c\ \omega\ R_u\ e^{\frac{k_1 \varphi}{c\ \omega} - \frac{k_1 \varphi_1}{c\ \omega}}\ (c\ \omega\ \cos(\varphi_1) + k_1 \sin(\varphi_1))}{c^2\omega^2 + k_1^2} + \\ & k_2\ (R_u \cos(\varphi) - R_l)) \end{aligned} \tag{3.38}$$

The distance to the center of the wheel was used to calculate the moment around the center of the wheel:

$$\Delta x(\varphi) = R_l\ tan(\varphi) \tag{3.39}$$

The resulting equation for the moment from the viscoelastic force:

$$M_{ve}(\varphi) = -F_{ve}(\varphi)\ \Delta x(\varphi) \tag{3.40}$$

Total contribution of the viscoelastic force in the z direction and moment around the centre of the wheel is the integral of $F_{ve}(\varphi)$ and $M_{ve}(\varphi)$. A primitive function can be derived for $F_{ve}(\varphi)$ but in order to derive a primitive function of $M_{ve}(\varphi)$ an approximation of $tan(\varphi) \approx sin(\varphi)$ is needed, this approximation is valid for small angles.

$$F_{ve,z} = \int_{\varphi_1}^{\varphi_2} F_{ve}(\varphi)\, d\varphi \tag{3.41}$$

$$M_{ve} = \int_{\varphi_1}^{\varphi_2} M_{ve}(\varphi)\, d\varphi \tag{3.42}$$

The angle φ_2 can be derived by solving equation 3.38 for $F_{ve}(\varphi_2) = 0$.

4

Identification of model parameters

In chapter 3 the bristle model was introduced with equations for the viscoelastic- and friction model. The bristle model contains five model parameters $k1$, $k2$, c, ρ, ζ. In this section, the procedure to collect rolling resistance data is presented along with two different methods to determine the model parameters. The parameters are to be valid for one tyre at one temperature but over the whole range of speeds and loads.

4.1 Rolling resistance measurements

VTI tyre testing facility is a flat track tyre testing rig which can be seen in figure 4.1. It is used to measure steering and braking forces on tyres during different conditions. A new measurement method has made it possible to measure the rolling resistance as well. It consists of a 50 meter long steel beam and a frame where a wheel can be mounted. When a measurement is conducted the frame pushes the wheel onto the steel beam as the beam is set into motion. There are different settings available such as changing the sideslip angle of the tyre, speed of the beam and surface of the beam among others. It is also possible to heat the tyre by rolling it against three small steel rolls while a normal force is applied. It is possible to measure the normal force (F_z), rolling resistance force (F_r) and the loaded tyre radius. With knowledge of the unloaded tyre radius and loaded tyre radius, the deformation (δ) can be calculated. RRM can be calculated by using equation 1.2.

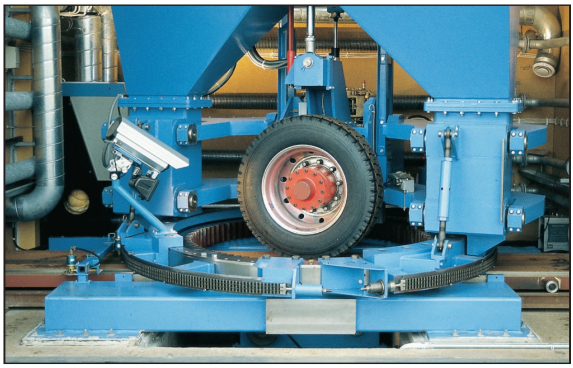

Figure 4.1: *A picture of the VTI's tyre testing facility.*

Measurements from five different load cases and three different speeds at two different inner tyre temperatures were collected for the two test tyres, a class B tyre and a class A tyre. The tyre pressure was set to 2800 *mBar* at an ambient temperature of around 18 °C. A limitation of the tyre rig was that it can achieve a maximum speed of 30 *km/h*. The tyre temperatures of interest were 20°C and 30°C which could coincide with the real tyre temperatures while driving a spring day in Linköping at both city and motorway, presented in chapter 2. The measurement data is presented in tables 4.2-4.3 and figures 4.2-4.6. For the load and speed cases where more than one measurement was collected an average value was used in the figures.

Table 4.1: *Measurement data for the A-class tyre, high temperatures.*

Speed = 1.7 km/h					
$RRM\ [Nm]$	$\delta\ [mm]$	$C_r\ [\cdot 10^{-3}]$	$F_z\ [N]$	Temperature [°C]	Comment
-4.71	13.8	4.56	2940	37.3	
-6.26	17.5	4.58	3935	36.6	
-7.99	20.8	4.79	4853	37.3	
-10.13	24.2	5.11	5815	34.7	
-11.15	27.4	4.83	6840	41.0	High temp.
Speed = 10 km/h					
$RRM\ [Nm]$	$\delta\ [mm]$	$C_r\ [\cdot 10^{-3}]$	$F_z\ [N]$	Temperature [°C]	Comment
-6.02	13.6	5.86	2923	34.3	
Speed = 30 km/h					
$RRM\ [Nm]$	$\delta\ [mm]$	$C_r\ [\cdot 10^{-3}]$	$F_z\ [N]$	Temperature [°C]	Comment
-6.73	13.4	6.53	2933	35.0	
-9.04	17.2	6.60	3942	33.9	
-10.67	20.4	6.39	4848	35.1	
-13.33	23.8	6.72	5809	34.1	
-15.33	27.1	6.66	6820	34.8	
-15.81	27.1	6.87	6816	33.8	

Table 4.2: *Measurement data for the A-class tyre, low temperatures.*

Speed = 1.7 km/h					
$RRM\ [Nm]$	$\delta\ [mm]$	$C_r\ [\cdot 10^{-3}]$	$F_z\ [N]$	Temperature [°C]	Comment
-5.45	14.3	5.32	2922	18.7	
-7.40	18.1	5.44	3922	17.8	
-9.25	21.6	5.60	4813	16.9	
-11.45	25.0	5.83	5781	16.6	
-13.20	28.3	5.79	6771	17.5	
Speed = 10 km/h					
$RRM\ [Nm]$	$\delta\ [mm]$	$C_r\ [\cdot 10^{-3}]$	$F_z\ [N]$	Temperature [°C]	Comment
-7.217	14.2	7.07	2910	15.9	
-9.678	18.0	7.14	3907	15.3	
-11.482	21.4	6.94	4809	15.3	
-13.499	24.8	6.90	5751	14.9	
-15.957	28.2	7.02	6751	16.1	
Speed = 30 km/h					
$RRM\ [Nm]$	$\delta\ [mm]$	$C_r\ [\cdot 10^{-3}]$	$F_z\ [N]$	Temperature [°C]	Comment
-8.37	13.9	8.21	2905	17.1	
-8.51	13.9	8.36	2899	16.9	
-8.58	13.9	8.44	2894	16.5	
-11.24	17.8	8.29	3906	15.1	
-13.25	21.2	8.02	4804	15.6	
-15.78	24.5	8.04	5765	14.9	
-18.26	28.0	8.00	6769	15.7	

Table 4.3: *Measurement data for the B-class tyre, high temperatures.*

Speed = 1.7 km/h					
$RRM\ [Nm]$	$\delta\ [mm]$	$C_r\ [\cdot 10^{-3}]$	$F_z\ [N]$	Temperature [°C]	Comment
-6.47	13.9	6.19	2959	37.6	
-8.93	17.5	6.46	3954	34.3	
-11.02	20.7	6.54	4868	37.7	
-11.06	20.7	6.55	4875	35.1	
-13.52	24.0	6.76	5827	37.8	
-16.27	27.2	7.00	6838	34.8	
Speed = 10 km/h					
$RRM\ [Nm]$	$\delta\ [mm]$	$C_r\ [\cdot 10^{-3}]$	$F_z\ [N]$	Temperature [°C]	Comment
-7.49	13.8	7.17	2956	35.0	
-9.98	17.4	7.21	3959	36.9	
-12.69	20.6	7.52	4870	36.0	
Speed = 30 km/h					
$RRM\ [Nm]$	$\delta\ [mm]$	$C_r\ [\cdot 10^{-3}]$	$F_z\ [N]$	Temperature [°C]	Comment
-8.53	13.5	8.20	2945	35.0	
-8.23	13.5	7.91	2944	35.1	
-11.33	17.1	8.15	3973	34.7	
-11.64	17.2	8.42	3954	30.1	
-14.23	20.3	8.42	4877	34.6	
-17.33	23.5	8.63	5845	34.3	
-17.61	23.5	8.78	5837	34.2	
-20.67	26.7	8.87	6845	34.2	
-20.16	26.7	8.66	6844	33.6	

Table 4.4: *Measurement data for the B-class tyre, low temperatures.*

Speed = 1.7 km/h					
$RRM\ [Nm]$	$\delta\ [mm]$	$C_r\ [\cdot 10^{-3}]$	$F_z\ [N]$	Temperature [°C]	Comment
-6.89	14.3	6.62	2953	17.2	
-9.60	18.0	6.98	3944	17.6	
-11.89	21.3	7.09	4851	missing data	
-14.50	24.6	7.29	5811	missing data	
-17.44	27.9	7.54	6824	missing data	
Speed = 10 km/h					
$RRM\ [Nm]$	$\delta\ [mm]$	$C_r\ [\cdot 10^{-3}]$	$F_z\ [N]$	Temperature [°C]	Comment
-9.27	14.0	9.06	2899	16.8	
-9.57	14.0	9.32	2910	17.9	
-9.37	14.0	9.16	2899	16.6	
-11.31	17.8	8.20	3948	16.3	
-14.02	21.0	8.36	4846	16.4	
-17.13	24.3	8.63	5794	17.2	
-20.63	27.7	8.93	6813	17.6	
Speed = 30 km/h					
$RRM\ [Nm]$	$\delta\ [mm]$	$C_r\ [\cdot 10^{-3}]$	$F_z\ [N]$	Temperature [°C]	Comment
-9.68	13.7	9.41	2910	18.4	
-9.71	13.7	9.42	2918	18.0	
-9.98	13.7	9.71	2910	17.6	
-13.26	17.4	9.66	3928	16.7	
-13.34	17.4	9.71	3932	17.2	
-13.28	17.4	9.68	3925	17.1	
-16.13	20.7	9.61	4845	17.3	
-16.42	20.7	9.79	4844	17.5	
-17.72	20.7	10.5	4849	17.6	Excluded
-19.55	24.0	9.83	5801	17.8	
-19.47	24.0	9.77	5810	18.2	
-19.42	24.0	9.75	5805	17.7	
-24.94	27.3	10.7	6826	17.7	Excluded
-23.17	27.2	10.0	6813	17.6	
-23.26	27.3	10.0	6818	17.7	

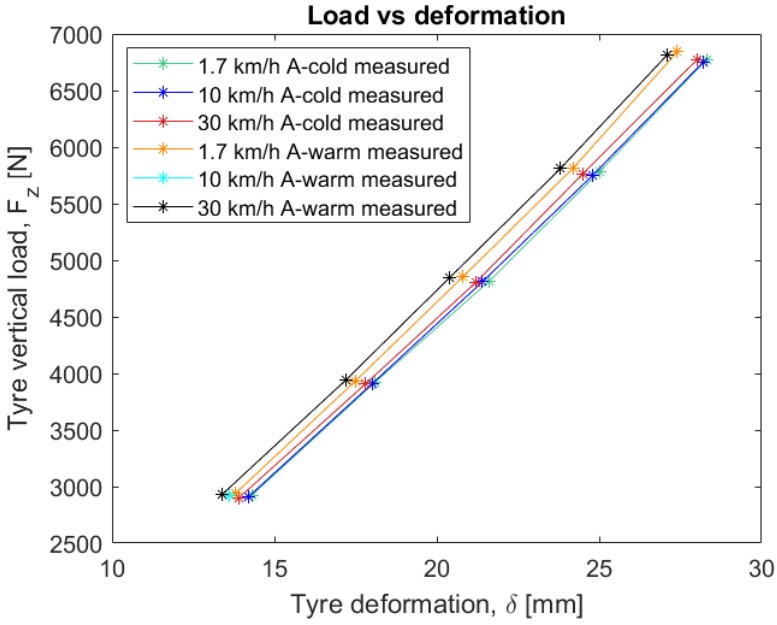

Figure 4.2: *Measured vertical force of the A-class tyre.*

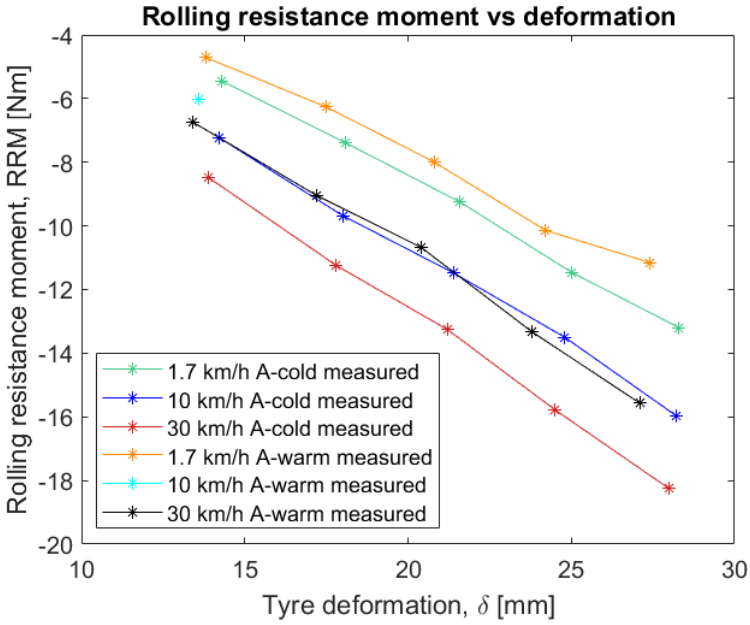

Figure 4.3: *Measured rolling resistance moment of the A-class tyre.*

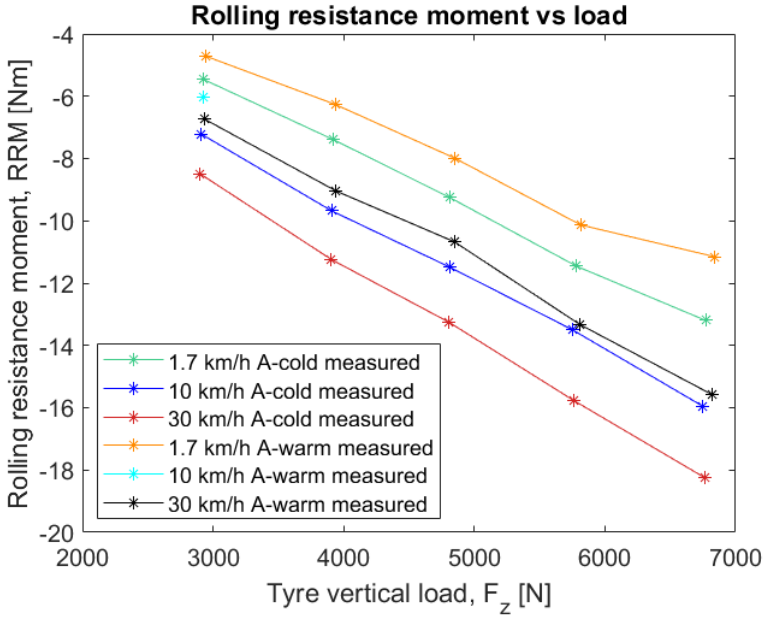

Figure 4.4: *Measured rolling resistance moment against load for the A-class tyre.*

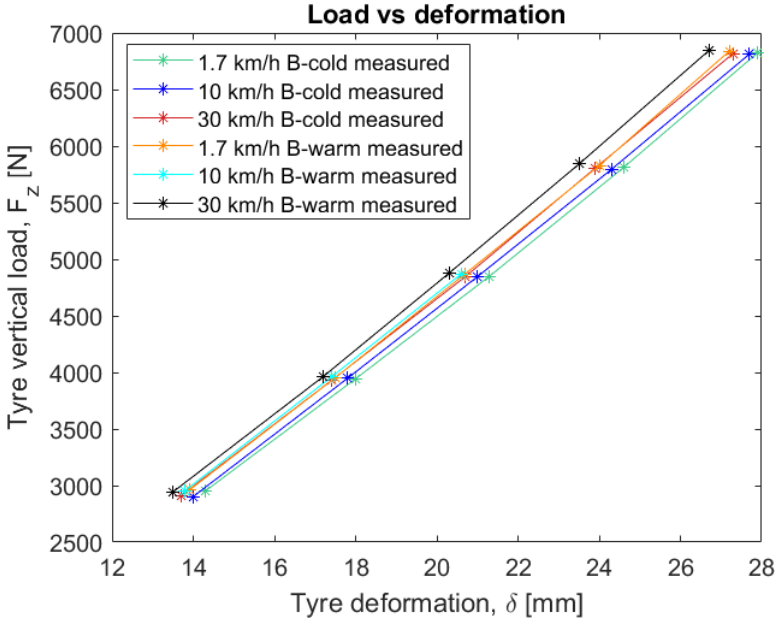

Figure 4.5: *Measured vertical force of the B-class tyre.*

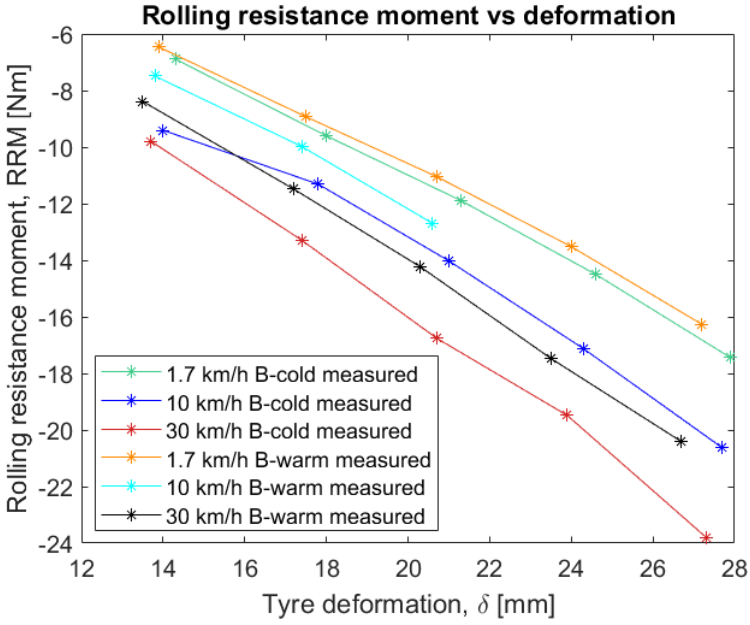

Figure 4.6: *Measured rolling resistance moment of the B-class tyre.*

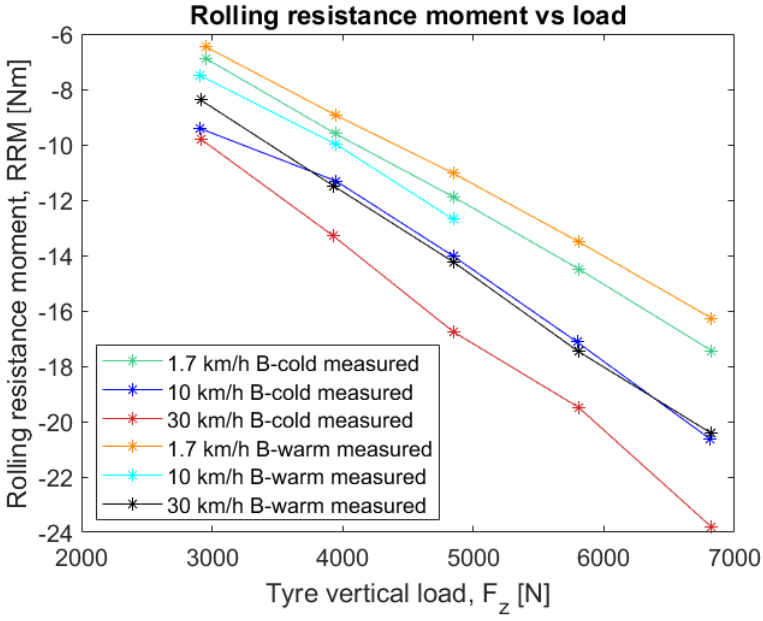

Figure 4.7: *Measured rolling resistance moment against load for the B-class tyre.*

The inner tyre temperature is difficult to control at the tyre rig which is why there is a temperature variation. The variation in temperature influences the rolling resistance moment measured which means that the reliability of the data is lowered. For instance in the data for the A-class tyre at high temperatures the highest load case have 6°C higher temperature at 1.7 *km/h* than at 30 *km/h*. The trend of increased rolling resistance by increased speed is to some degree increased by the effect of decreased rolling resistance at higher temperatures. Some measurements had a variation in speed and were excluded from the figures presented here and when optimising the model parameters. Several measurements were done multiple times and an average value was calculated to get more reliable results.

The trends seen in the measurement data correlates well with findings of others in literature [12] [7]. However, some measurements stand out and can not be explained. In figure 4.6 for the cold B-class tyre at 10 *km/h*, it was observed that the rolling resistance moment at the lowest load does not follow the trend. The data point for the lowest load is an average of three measurements, which implies that it is not just a measurement error. Nothing with the conditions of these measurements can explain this deviating behaviour. This trend is only observed for that specific case.

4.2 Identification of parameters by dividing the model

The reason behind this method was that optimising all parameters at once appeared to be difficult. In this method the bristle model is divided, first the parameters of one part is optimised, then the parameters for the second part is optimised.

4.2.1 Parameter k_2, ρ and ζ

To identify the parameters k_2, ρ and ζ the viscous effect is assumed to be negligible at the lowest speed. When the tyre has low speed the effect from viscous effect is disconnected in the Zener model, hence only the elastic spring remains. The influence of friction is still present, this leads to a rubber model consisting of a spring in series with a Jenkins element, see figure 4.8. The viscous effect has to be parametrised to be negligible at a lower speed for this to be valid. If the viscous effect is present at a lower speed it is important to note that the contact patch of the tyre changes which alters the contribution from the internal friction.

Only the model parameters k_2, ρ and ζ are present in the simplified bristle model. The optimal model parameters $\hat{\rho}$, $\hat{\zeta}$ and $\hat{k}_2$ were determined by the use of parameter estimation. In equation 4.1, g is the cost function according to equation 4.2. L is the number of data points (points presented in the graphs in section 4.1) available for the tyre at low speeds for each temperature case. It was necessary to weigh the force and moment in the cost function since they are of different magnitude, this was done by dividing with the mean value of the force respectively the moment.

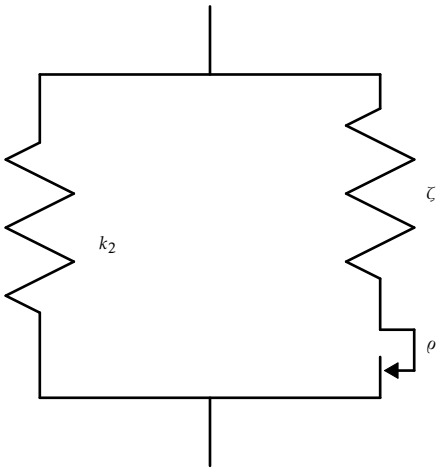

Figure 4.8: *Simplified bristle model that is used for parameter identification at low speeds.*

$$\hat{k}_2, \hat{\rho}, \hat{\zeta} = \underset{k_2,\rho,\zeta}{\arg\min}\, g(k_2, \rho, \zeta) \tag{4.1}$$

$$g = \sum_{n=1}^{L} \left(\frac{F_{z,n} - \hat{F}_{z,n}}{F_{z,mean}} \right)^2 + \sum_{n=1}^{L} \left(\frac{RRM_n - R\hat{R}M_n}{RRM_{mean}} \right)^2 \tag{4.2}$$

With the simplified bristle model, it is possible to calculate $\hat{F}_z$ and $R\hat{R}m$ for varying speeds and loads. The only input needed is the loaded tyre radius and speed. The cost function runs for different values of k_2, ρ and ζ, the combination that minimises the difference between the measured and modelled value for the total force and total moment are the optimal model parameters for the bristle model. Testing a lot of different values is time-consuming which is why the Matlab function *fminsearchbnd* was used. It optimises the parameters and finds a local minimum. Since a local minimum might not coincide with the global minimum, different starting parameters were tested.

4.2.2 Parameter k_1 and c

At higher speeds both the viscoelastic and internal friction are present. After the model parameters k_2, ρ and ζ had been determined as described in section 4.2.1 only two unknown parameters remain, k_1 and c. A similar approach was used for identifying the last two parameters, see equation 4.3 and 4.4.

$$\hat{k}_1, \hat{c} = \underset{k_1,c}{\arg\min}\, g(k_1, c) \tag{4.3}$$

$$g = \sum_{n=1}^{K} \left(\frac{F_{z,n} - \hat{F}_{z,ve,n}}{F_{z,mean}} \right)^2 + \sum_{n=1}^{K} \left(\frac{RRM_n - \hat{M}_{f,n} - \hat{M}_{ve,n}}{RRM_{mean}} \right)^2 \tag{4.4}$$

K is the number of data points available for the tyre at each temperature case. $F_{z,n}$ is the measured force at data point n and RRM_n is the measured moment at the data point n. The internal friction is frequency independent which means that it is constant for all speeds. After the parameters k_2, ρ and ζ were identified this moment of force was known and is here denoted $\hat{M}_{f,n}$ for data point n. It is the modelled moment of the internal friction.

$\hat{F}_{z,ve,n}$ and $\hat{M}_{ve,n}$ is the modelled viscoelastic force and moment. By using the analytical model this part can be modelled separately. The calculation for the angle φ_2 has to be altered since the force from the internal friction is not taken into account. The force from the internal friction is not large in total since it is positive at the beginning of the contact patch and negative at the end of the contact patch. It does however influence the angle φ_2 which is the angle to where the force at the contact patch becomes equal to zero. It is compensated by solving equation 3.38 for $F_{ve}(\varphi_2) = \rho$ instead of $F_{ve}(\varphi_2) = 0$.

4.3 Identification of parameters with the complete model

By using the complete model the viscoelastic model was allowed to contribute to the moment and force even at low speeds. Optimising all parameters to fit the measurement data was performed with equation 4.5 and 4.6 together with the Matlab function *fminsearchbnd*. K is the total number of data points available for the tyre at each temperature case. Since a local minimum might be found which not coincide with the global minimum several different starting points were tested.

$$\hat{k}_2, \hat{\rho}, \hat{\zeta}, \hat{k}_1, \hat{c} = \underset{k_2,\rho,\zeta,k_1,c}{\arg\min}\, g(k_2, \rho, \zeta, k_1, c) \tag{4.5}$$

$$g = \sum_{n=1}^{K} \left(\frac{F_{z,n} - \hat{F}_{z,n}}{F_{z,mean}} \right)^2 + \sum_{n=1}^{K} \left(\frac{RRM_n - \hat{RRM}_n}{RRM_{mean}} \right)^2 \tag{4.6}$$

4.4 Discussion of the methods

The reason for developing the method with a divided model was that using the complete model and identifying all parameters at once was expected to be difficult. Dividing the model into two has several setbacks compared to using the complete model. The major one is that the parameters of the viscoelastic model need to be set in a way that makes the contribution negligible at low speeds. Both methods were tested but the method of using the complete model gave the best results which is why the results from this method are presented in chapter 5.

5
Results

In this chapter, the result from the optimisation of the complete model is presented. The result consists of the optimised parameters (k_2, ρ, ζ, k_1, c) and comparisons between measurements and model.

5.1 Comparison between measurements and model

To evaluate the model a comparison between the measurements and model was made. For each tyre class and temperature case, the measured deformation δ was plotted against F_z and the RRM, as well as a plot of RRM against F_z. The outcome are presented in figures 5.4 - 5.9. For the two cases, A-class - warm and B-class - warm, measurements for all loads were not collected for the speed 10 km/h. The complete model has the loaded tyre radius as input, also mentioned in section 4.1, therefore, to show the model for these cases over the whole range of loads an average of the loaded tyre radius for the 1.7 km/h and 30 km/h was used for concerned loads.

How well the model fit the measurement data is also presented with the mean square error, MSE, which is found in table 5.1. The mean square error is calculated according to equation 5.1 for the force and in the same way for both the moment and deformation. The modelled deformation is obtained by using a normal force as input to the model and comparing the measured loaded tyre radius with the modelled value. In order to get a total weighted MSE, all MSE values are weighed with the mean measured value of the force/ moment/ loaded tyre

radius powered to two and summarised.

$$\sum_{m=1}^{K} (F_{z,m} - \hat{F}_{z,m})^2 \tag{5.1}$$

Table 5.1: *Mean square error of F_z, RRM, R_l and a total weighted MSE.*

Case	F_z MSE	RRM MSE	R_l MSE	total MSE
A-class cold	67350	0.27	$7.4 \cdot 10^{-7}$	$4.9 \cdot 10^{-3}$
A-class warm	305624	0.14	$1.8 \cdot 10^{-6}$	$2.9 \cdot 10^{-2}$
B-class cold	55539	0.30	$5.7 \cdot 10^{-7}$	$3.8 \cdot 10^{-3}$
B-class warm	58861	0.06	$5.2 \cdot 10^{-7}$	$4.2 \cdot 10^{-3}$

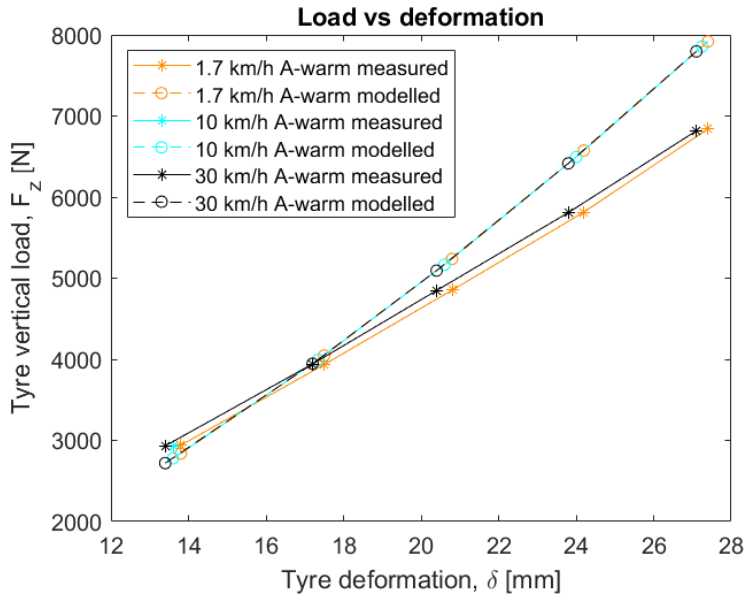

Figure 5.1: *Shows the measured and modelled load against deformation for the warm A-class tyre.*

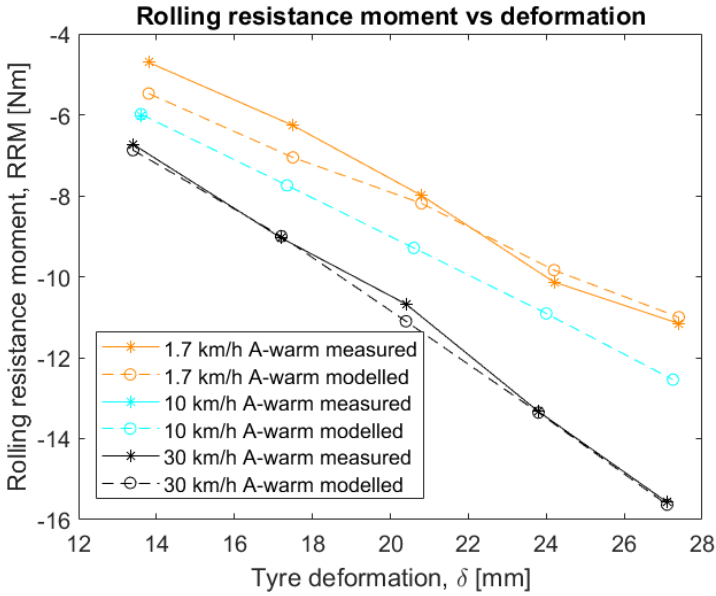

Figure 5.2: *Shows the measured and modelled rolling resistance moment against deformation for the warm A-class tyre.*

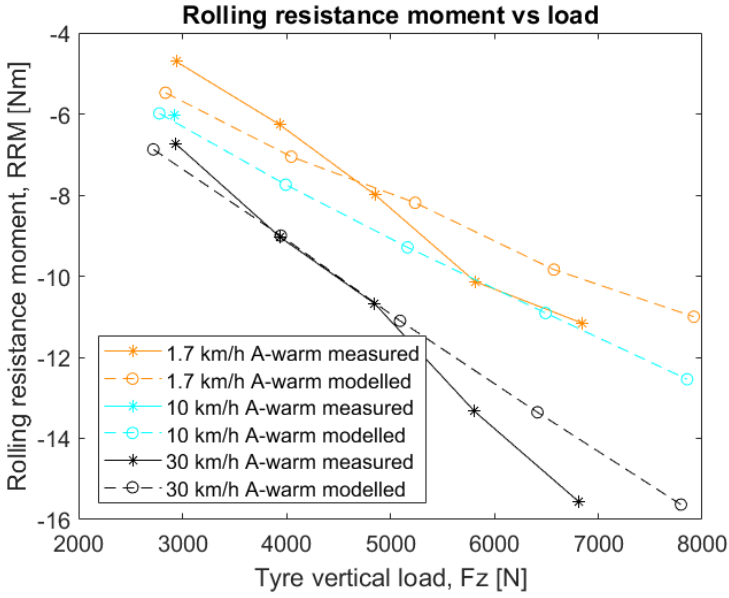

Figure 5.3: *Shows the measured and modelled rolling resistance moment against load for the warm A-class tyre.*

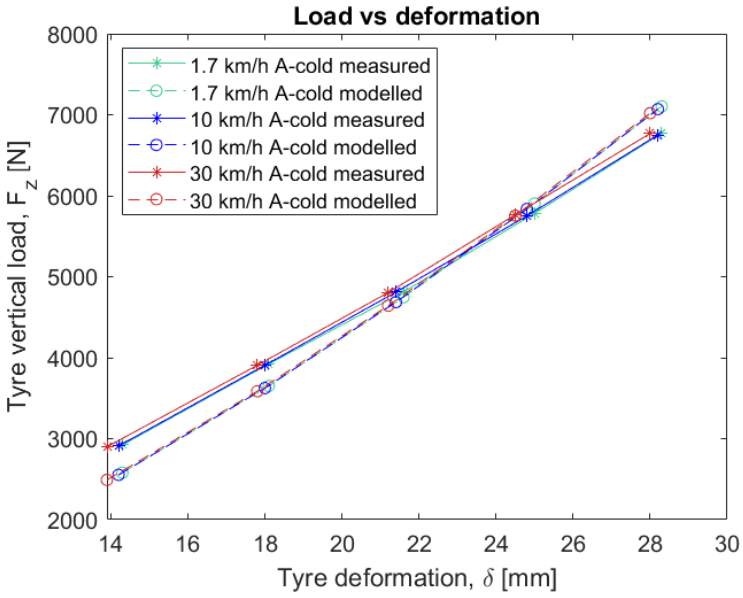

Figure 5.4: *Shows the measured and modelled load against deformation for the cold A-class tyre.*

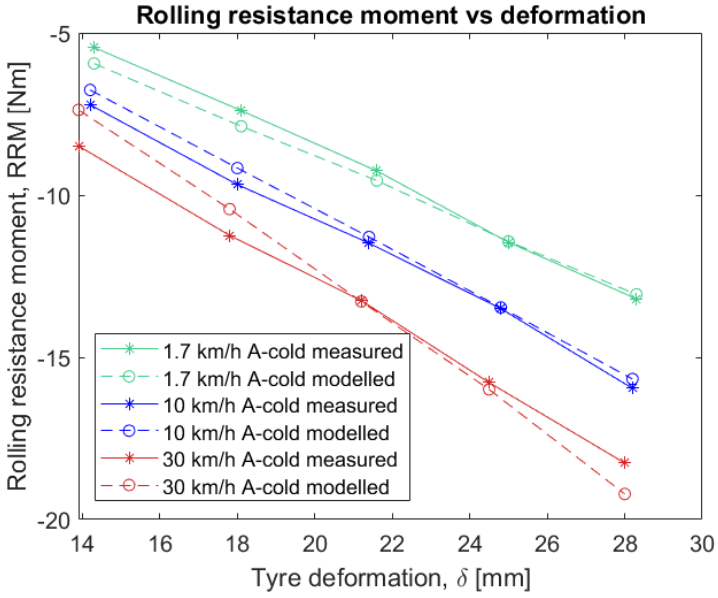

Figure 5.5: *Shows the measured and modelled rolling resistance moment against deformation for the cold A-class tyre.*

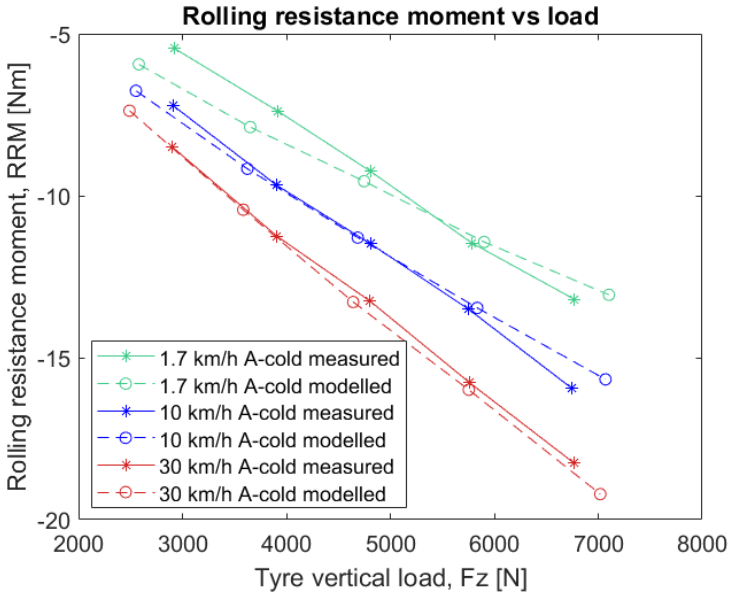

Figure 5.6: *Shows the measured and modelled rolling resistance moment against load for the cold A-class tyre.*

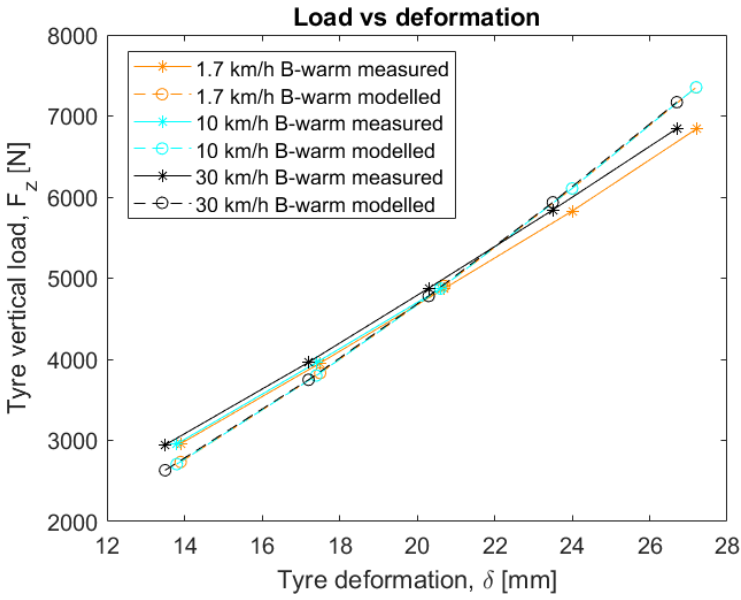

Figure 5.7: *Shows the measured and modelled load against deformation for the warm B-class tyre.*

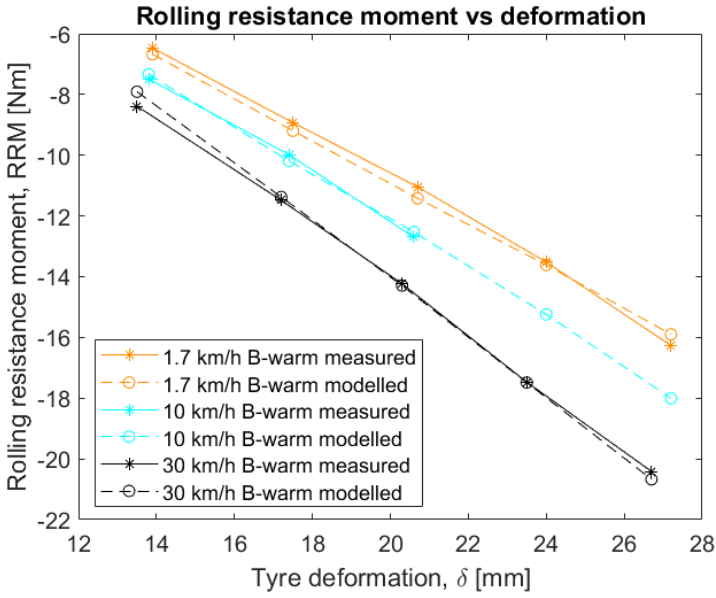

Figure 5.8: *Shows the measured and modelled rolling resistance moment against deformation for the warm B-class tyre.*

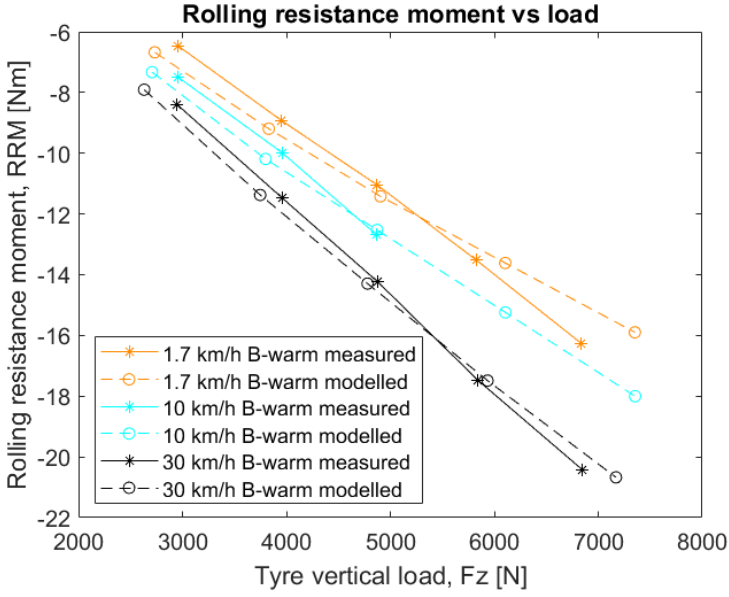

Figure 5.9: *Shows the measured and modelled rolling resistance moment against load for the warm B-class tyre.*

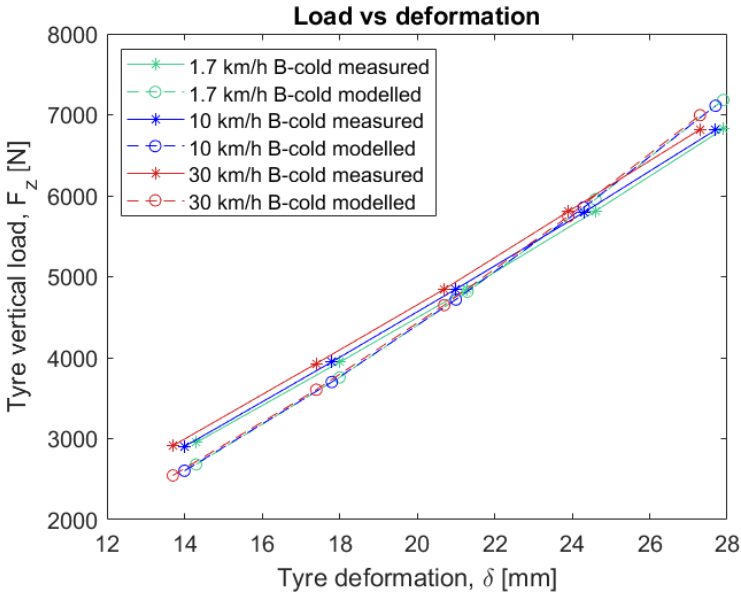

Figure 5.10: *Shows the measured and modelled load against deformation for the cold B-class tyre.*

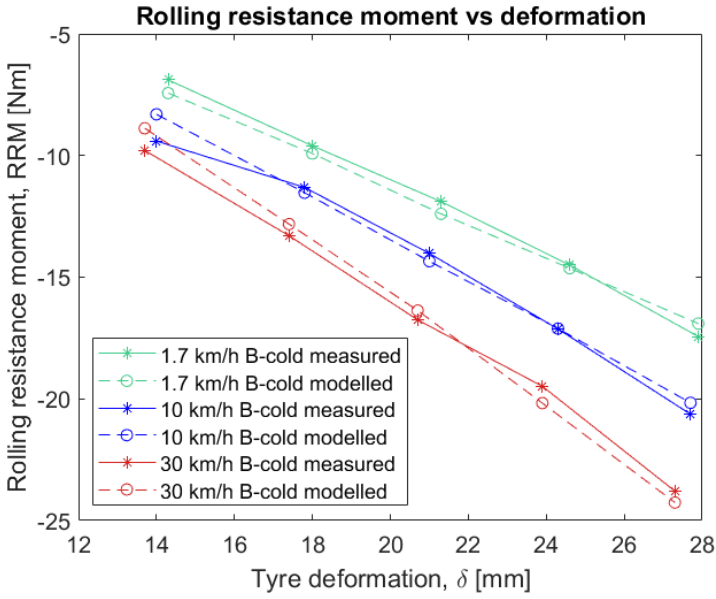

Figure 5.11: *Shows the measured and modelled rolling resistance moment against deformation for the cold B-class tyre.*

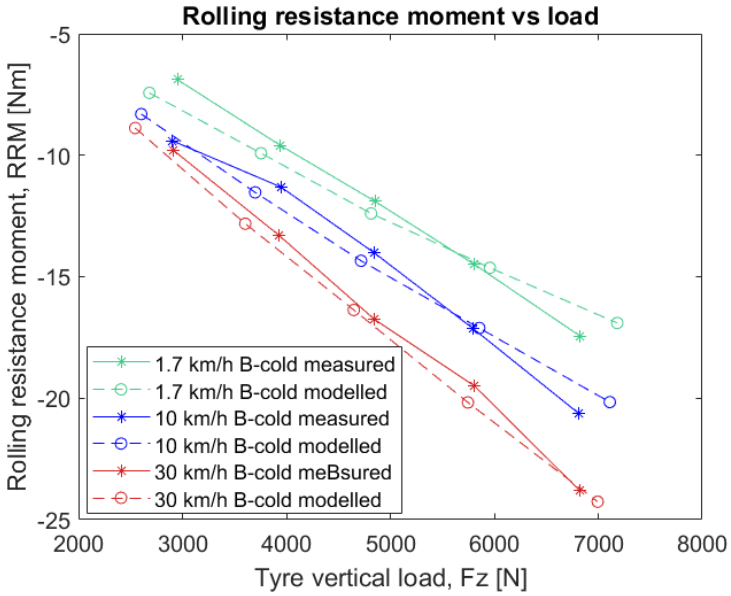

Figure 5.12: *Shows the measured and modelled rolling resistance moment against load for the cold B-class tyre.*

5.2 Optimised parameters

The optimisation of the parameters for the complete model was executed as presented in 4.3. The resulting optimised parameters are presented in table 5.2. When running the complete model the number of bristles was set to 150.

Table 5.2: *Parameters used in the complete brush model.*

Case	k_2	ρ	ζ	k_1	c
A class - cold	4952	2.639	1295	970.2	0.958
A class - warm	5822	2.175	5089	4264	0.515
B class - cold	5106	3.674	1201	1022	1.280
B class - warm	5429	3.651	1080	1313	0.753

6
Discussion

By analysing the measured and modelled force it can be seen that the measurements do not coincide well across all loads. The reason for this can be explained by looking into the low-speed case when the tyre is almost at standstill. The deformed area of the tyre should be linear to the force in this case. By comparing the deformed area as a function of the deformation δ with the measurements the problem become clear. In figure 6.1 the modelled deformed area is plotted (and scaled with a constant factor) with the measured values of the deformation and the force.

From the plots of the force, it is clear that an increase in speed yields a higher stiffness of the tyre. The viscoelastic part can alter the tyre stiffness at different speeds which should make it possible to fit the parameters to the force measurements. However the moment is also influenced, the parameters therefore need to be adapted to fit both the moment and the force. A change in the parameters k_1 and c have a small impact on the force but a large impact on the moment. The optimisation of the parameters using the cost function described in section 4.3 therefore result in a good fit of the measured and modelled moment while the increase in stiffness at higher speeds is not taken into account.

The modelled value of the moment coincide well with the measured value of the moment as can be seen in figure 5.2, 5.5, 5.8 and 5.11 when the loaded tyre radius is used as input. All measurement points are not captured perfectly but the general behaviour of increased moment with increased speed and load is represented well. There is an uncertainty in the measurement data as well which possibly could be a reason for the model not fitting the data better. Data at higher speeds needs to be collected and analysed to see if the model is valid at higher speeds. In this thesis only speeds up to 30 *km/h* have been tested.

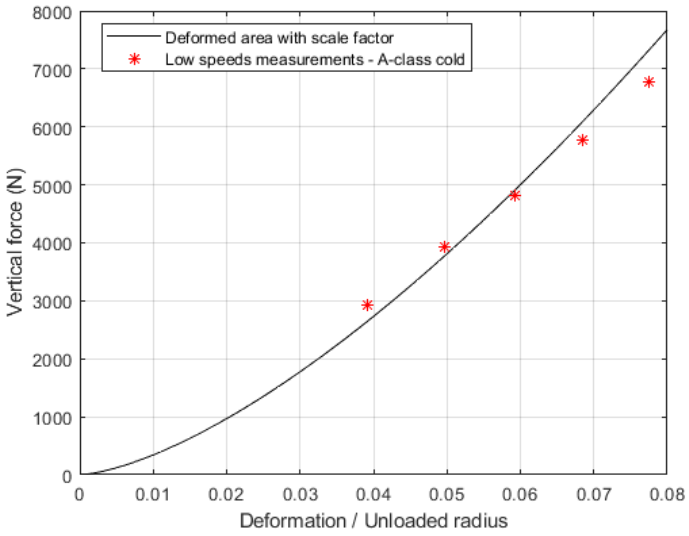

Figure 6.1: *Modelled deformed area against deformation and measured force against deformation.*

The figures 5.3, 5.6, 5.9 and 5.12 show the modelled rolling resistance moment against the modelled load. Good agreement for the moment and worse agreement for the load can be observed. If the load is used as input to the model, the resulting moment will contain an error. By analysing the cold B-class tyre at 30 *km/h* with load as input the result in table 6.1 is obtained.

Table 6.1: *Modelled and measured RRM with force as input to the model.*

Load [N]	Modelled RRM [Nm]	Measured RRM [Nm]	Error [Nm]
3000	-10.7	-9.8	0.7
3970	-14.3	-13.3	1
4910	-17.7	-16.8	0.9
5900	-21.3	-19.5	1.8
6970	-25.2	-23.8	1.4

As can be seen in table 5.1 the best fit was found for the cold B-class tyre and the worst fit was found for the warm A-class tyre. A possible explanation to this could be the temperature variation for the warm A-class tyre which is discussed in section 4.1. For the warm A-class tyre there was also fewest data points available compared to the cold B-class tyre which had the most data points available. It is also noted that the RRM fits best for warm tyres, which should be investigated. Since the characteristics change between a warm and a cold tyre it is possible that the model fit a warm tyre better.

The effective rolling radius was approximated by using equation 3.1. At the VTI tyre testing facility, the angular velocity is measured together with the speed of the steel beam. This gives the possibility to compare the modelled effective rolling radius with the real effective rolling radius. Results show that the approximation of the effective rolling radius can be improved. From the measurement of the cold A-class tyre at low speed and low load, the effective rolling radius is 358 *mm* while it is approximated to 337 *mm* in the model.

The bristles are as of now modelled to only deform in the z-direction and therefore only yields forces in the z-direction. A possible improvement that can be made to the model is to change the deformation of the bristles according to figure 6.2 where the bristles are angled to connect to the center of the wheel instead of perpendicular to the surface. In this case there would be deformation and forces in both the z- and x-direction which could yield better results.

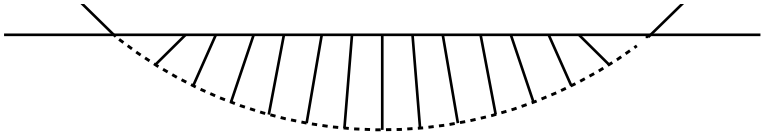

Figure 6.2: *Illustration of an alternative bristle deformation.*

7

Summary

This chapter presents the conclusions of the work carried out in the thesis and suggestion for future work.

7.1 Summary and conclusion

Temperature measurements were carried out around Linköping at several different conditions. Different weather conditions and different routes were tested. A clear picture of how the inner tyre temperature varies is presented for ambient temperatures around 0°C to 24°C. The inner tyre temperature for the rear tyres varies between 11°C to 36°C for these ambient conditions while the inner tyre temperature for the front tyres is higher due to the front-wheel-drive of the car.

A tyre model which models the vertical force F_z and rolling resistance moment RRM was also developed. The model is a brush model with the bristles modelled to represent both the internal friction of the tyre and the viscoelastic characteristics. The viscoelastic model was created as a discrete model where the bristles were updated with a time step τ and as an analytical model which resulted in a mathematical expression for both the force and the moment on the tyre.

Measurement data was collected in a test rig for different tyre temperatures, speeds and loads. The parameters of the created model were then fitted to this measurement data. Comparisons between the model and measurements show that the model represents the rolling resistance moment rather well. So the model concept has a potential but improvements need to be made to capture the behaviour of the force better.

7.2 Recommendations for future work

It would be interesting to continue to collect temperature measurement data over a wider range of ambient temperatures and conditions to be able to see the whole temperature range passenger car tyres operates within. This is an area that is missing in literature since companies and researchers main focus is on lab environment standardised testing. The actual tyre temperatures in real driving for a broader spectrum would help in the modelling process, it would also give knowledge for how the temperatures achieved in the lab environment correlates to reality. Tyres from more classes and different manufacturers should also be tested.

A better understanding of how the force and moment change on the tyre with an increase in speed or load is needed. Therefore more measurements are needed over a wider range of speeds and loads. From the collected data a better understanding of what should be altered within the model can be achieved. As of now, the created model is only tested up to 30 *km/h*, with data collected at higher speeds more thorough tests of the model could be made.

There are other viscoelastic and internal friction models available that have not been tested within this thesis that could be investigated. As of now a stiff carcass on which the bristles are placed are used, with a flexible carcass a more accurate model might be obtained, it could solve the problem described in figure 6.1. An implementation of a flexible carcass could therefore be tested. The alternative deformation of the bristles presented in figure 6.2 would also be of interest. Efforts could also be put into finding a better way to describe the effective rolling radius.

By investigating the tyres at a wider range of temperatures a function that alters the model parameters depending on tyre temperature could also be investigated.

Appendix

A

Solution to the viscoelastic model

In this appendix the solution to express the viscoelastic model in the time domain, equation 3.14, by using equations 3.8 - 3.13 is presented.

Equation 3.9, 3.11 and 3.12 are used to get equation A.1 and A.2.

$$\dot{\delta}_{k_1}(t) = \frac{\dot{F}_v(t)}{k_1} \tag{A.1}$$

$$\dot{\delta}_c(t) = \frac{F_v(t)}{c} \tag{A.2}$$

Equation 3.13 can be used to get equation A.3.

$$\dot{\delta}_c(t) + \dot{\delta}_{k_1}(t) = \dot{\delta}(t) \tag{A.3}$$

Equation A.1 and A.2 in equation A.3 gives:

$$\dot{\delta}(t) = \frac{\dot{F}_v(t)}{k_1} + \frac{F_v(t)}{c} \tag{A.4}$$

By using Laplace transform at equation A.4:

$$F_v = \frac{s\,\delta}{\frac{s}{k_1} + \frac{1}{c}} \tag{A.5}$$

Equation 3.8 and A.5 give:

$$\frac{s\,\delta}{\frac{s}{k_1}\frac{1}{c}} + k_2\delta = F_{ve} \tag{A.6}$$

Simplification gives:

$$s\,F_{ve} = -F_{ve}\frac{k_1}{c} + \frac{k_1 k_2}{c}\delta + s\,\delta(k_1 + k_2) \tag{A.7}$$

By using inverse Laplace transform at equation A.7, equation 3.14 is achieved.

B

Solution to the differential equation

In this appendix the solution for the differential equation of δ_{k_1} is presented, see equation B.1.

$$-\omega\delta'_{k_1}(\varphi) + \frac{k_1}{c}\delta_{k_1}(\varphi) = \omega R_u sin(\varphi) \tag{B.1}$$

By dividing by $-\omega$ the integrating factor for the differential equation becomes:

$$e^{\frac{-k_1\varphi}{c\omega}} \tag{B.2}$$

Leading to the following expression:

$$\delta'_{k_1}(\varphi)e^{\frac{-k_1\varphi}{c\omega}} - \frac{k_1}{c\omega}e^{\frac{-k_1\varphi}{c\omega}}\delta_{k_1}(\varphi) = -R_u\sin(\varphi)e^{\frac{-k_1\varphi}{c\omega}} \tag{B.3}$$

The left hand-side of the equation can be rewritten as:

$$\delta'_{k_1}(\varphi)e^{\frac{-k_1\varphi}{c\omega}} - \frac{k_1}{c\omega}e^{\frac{-k_1\varphi}{c\omega}}\delta_{k_1}(\varphi) = (\delta_{k_1}(\varphi)e^{\frac{-k_1\varphi}{c\omega}})' \tag{B.4}$$

Resulting in:

$$\left(\delta_{k_1}(\varphi)e^{\frac{-k_1\varphi}{c\omega}}\right)' = -R_u\sin(\varphi)e^{\frac{-k_1\varphi}{c\omega}} \tag{B.5}$$

Integrating both sides:

$$\delta_{k_1}(\varphi)e^{\frac{-k_1\varphi}{c\omega}} = \int -R_u\sin(\varphi)e^{\frac{-k_1\varphi}{c\omega}}\,d\varphi \tag{B.6}$$

After two partial integration's the term $\int \sin(\varphi) e^{\frac{-k_1\varphi}{c\omega}}\, d\varphi$ appear again and the integral can be solved.

$$\begin{aligned}\delta_{k_1}(\varphi) e^{\frac{-k_1\varphi}{c\omega}} = R_u \Bigg(& \frac{c\omega}{k_1} e^{\frac{-k_1\varphi}{c\omega}} \sin(\varphi) - \frac{c^2\omega^2}{k_1^2} e^{\frac{-k_1\varphi}{c\omega}} \cos(\varphi) + \\ & \frac{c^2\omega^2}{c^2\omega^2 + k_1^2} \left(\frac{c^2\omega^2}{k_1^2} e^{\frac{-k_1\varphi}{c\omega}} \cos(\varphi) - \frac{c\omega}{k_1} e^{\frac{-k_1\varphi}{c\omega}} \sin(\varphi) \right) \Bigg) + C_1\end{aligned} \tag{B.7}$$

Simplification gives:

$$\delta_{k_1}(\varphi) = \frac{c\omega R_u \left(c\omega \cos(\varphi) + k_1 \sin(\varphi)\right)}{c^2\omega^2 + k_1^2} + C_1 e^{\frac{k_1\varphi}{c\omega}} \tag{B.8}$$

As presented in equation 3.36. The arbitrary constant can be derived from the condition that there is no deformation just as the contact patch is entered, $\delta_{k_1}(\varphi_1) = 0$.

$$0 = \frac{c\omega R_u \left(c\omega \cos(\varphi_1) + k_1 \sin(\varphi_1)\right)}{c^2\omega^2 + k_1^2} + C_1 e^{\frac{k_1\varphi_1}{c\omega}} \tag{B.9}$$

$$C_1 = -\frac{c\omega R_u e^{-\frac{k_1\varphi_1}{c\omega}} \left(c\omega \cos\left(\varphi_1\right) + k_1 \sin\left(\varphi_1\right)\right)}{c^2\omega^2 + k_1^2} \tag{B.10}$$

The final expression for $\delta_{k_1}(\varphi)$ becomes:

$$\delta_{k_1}(\varphi) = \frac{c\omega R_u \left(c\omega \cos(\varphi) + k_1 \sin(\varphi)\right)}{c^2\omega^2 + k_1^2} - \frac{c\omega R_u \left(c\omega \cos\left(\varphi_1\right) + k_1 \sin\left(\varphi_1\right)\right)}{c^2\omega^2 + k_1^2} \tag{B.11}$$

Bibliography

[1] Michelin Clermont-Ferrand. The tyre: Rolling resistance and fuel savings, 2003.

[2] Francesco Conte. Expanding the brush tire model for energy studies, 2014.

[3] J. Crank and P. Nicolson. A practical method for numerical evaluation of solutions of partial differential equations of the heat-conduction type. *Mathematical Proceedings of the Cambridge Philosophical Society*, 43(1):50–67, 1947. doi: 10.1017/S0305004100023197.

[4] Mohammad Mehdi Davari. *A tyre model for energy studies in vehicle dynamics simulations*. PhD thesis, KTH Royal Institute of Technology, 2015.

[5] European Environment Agency European Commission, DG Climate Action. Annual european union greenhouse gas inventory 1990–2018 and inventory report 2020. page 91, 2020.

[6] National Research Council (US). Transportation Research Board. Committee for the National Tire Efficiency Study. *Tires and passenger vehicle fuel economy: informing consumers, improving performance*, volume 286. Transportation Research Board, 2006.

[7] David E Hall and J Cal Moreland. Fundamentals of rolling resistance. *Rubber chemistry and technology*, 74(3):525–539, 2001.

[8] Izze-Racing. Sensors, 2021. URL `http://www.izzeracing.com/products-page.html`.

[9] WV Mars and JR Luchini. An analytical model for the transient rolling resistance behavior of tires. *Tire Science and Technology*, 27(3):161–175, 1999.

[10] Desmond F Moore. The friction of pneumatic tyres. 1975.

[11] Y. Nakajima. *Rolling Resistance of Tires*. Springer, 2019. ISBN 978-981-13-5799-2.

[12] Lars Nielsen and Tony Sandberg. A new model for rolling resistance of pneumatic tires. *SAE Transactions*, pages 1572–1579, 2002.

[13] SAEJ670e. Vehicle dynamics terminology. *Society of Automotive Engineers, Inc*, 1976.

[14] Michael Sayers. Standard terminology for vehicle dynamics simulations. *The University of Michigan Transportation Research Institute (UMTRI), Tech. Rep*, 1996.

[15] DJ Schuring. The rolling loss of pneumatic tires. *Rubber chemistry and technology*, 53(3):600–727, 1980.

[16] LaClair T.J. *Rolling resistnace. In Gent AN and Walter JD (eds) The Pneumatic Tire*. Washington: NHTSA, 1 edition, 2006.

[17] Trafikverket. Pmsv3, 2021. URL `https://pmsv3.trafikverket.se/Pages/StrackaUrval/StrackaUrvalView.aspx`.

[18] J. Y. Wong. *Theory of Ground Vehicles*. John Wiley & Sons Inc., 3 edition, 2001.

[19] Kazutaka Yokota, Eisei Higuchi, and Masashi Kitagawa. Estimation of tire temperature distribution and rolling resistance under running conditions including environmental factors. Technical report, SAE Technical Paper, 2012.